ABSTRACT

Title of Thesis:	FLUORESCENT ULTRASHORT NANOTUBES FROM DEFECT-INDUCED CHEMICAL CUTTING
	Yunfeng Li, Master of Science, 2020
Thesis Directed By:	Professor YuHuang Wang Department of Chemistry and Biochemistry

Ultrashort single-walled carbon nanotubes (SWCNTs) that fluoresce brightly in the shortwave infrared shows great potentials in bioimaging, sensing and enabling room-temperature, solid-state single-photon sources. However, this novel family of materials remains largely unexplored due to the synthetic challenge. In this thesis, I will introduce a high-yield synthesis method of fluorescent ultrashort nanotubes based on a fundamental new understanding of defect-induced chemical cutting of SWCNTs. The method includes implanting fluorescent quantum defects onto the carbon nanotubes, and then cutting the nanotubes preferentially from the defect sites. Firstly, I demonstrate that this simple two-step process leads to the synthesis of ultrashort nanotubes with a narrow length distribution and fluorescence in the shortwave infrared. Then, I will further elucidate the mechanism of this defect-induced chemical cutting at the molecular level for the first time by in-situ monitoring the spectral fingerprint of the nanotube and the fluorescent quantum defect as the reaction proceeds. This thesis

reveals fundamental insights in defect chemistry and makes fluorescent ultrashort nanotubes synthetically accessible for both basic and applied studies.

FLUORESCENT ULTRASHORT NANOTUBES FROM DEFECT-INDUCED CHEMICAL CUTTING

by

Yunfeng Li

Thesis submitted to the Faculty of the Graduate School of the
University of Maryland, College Park, in partial fulfillment
of the requirements for the degree of
Master of Science
2020

Advisory Committee:
Professor YuHuang Wang, Chair
Professor Sang Bok Lee
Assistant Professor Leah G. Dodson

© Copyright by
Yunfeng Li
2020

Acknowledgements

First of all, I feel grateful to my advisor Dr. YuHuang Wang for his strong support over the past four years. I appreciate the great opportunity to work in the Wang research lab and his valuable advice in guiding my research.

I also feel so blessed to work in a research team full of love and kindness. Among all my teammates, I would like to especially thank Dr. Xiaojian Wu, Dr. Peng Wang, Dr. Mijin Kim, Haoran Qu, Jacob Fortner, Zachery Rizer and Dr. Jacek Klos. All of my research progress and publications rely on their constructive advice, helpful discussions and selfless assistance.

I would like to thank my committee members Dr. Sang Bok Lee and Dr. Leah Dodson for their support and advice on my thesis and graduation.

I would also like to thank Dr. Alexandra Brozena and Zachery Rizer for their constructive input in revising this thesis.

Lastly, I appreciate my parents for their love and care.

Table of Contents

Acknowledgements i
Table of Contents ii
List of Abbreviations iv
Chapter 1: Fluorescent Ultrashort Nanotubes 1
1.1 Introduction to Single-Walled Carbon Nanotubes 1
1.2 Fluorescent Ultrashort Nanotubes: Potentials and Significance 2
1.2.1 Biocompatible Emitters in Bioimaging and Sensing 2
1.2.2 Efficient Single-Photon Sources 4
1.3 Fluorescent Quantum Defects Enable Ultrashort Nanotubes to Fluoresce 5
1.4 Synthesis of Ultrashort Nanotubes 6
1.4.1 Mechanical Cutting: Tip Sonication 7
1.4.2 Chemical Cutting: Oxidative Cutting 8
1.5 Synthetic Challenges Addressed in this Thesis 10
Chapter 2: Synthesizing Fluorescent Ultrashort Nanotubes from Defect-Induced Chemical Cutting 12
2.1 Introduction 12
2.2 Experimental Methods 13
2.2.1 Implanting sp^3 Defects in SWCNTs 13
2.2.2 Cutting f-SWCNTs in H_2O_2 14
2.2.3 Alternative Approach of Defect Implanting for DICE 15
2.2.4 Spectroscopic Characterization of Fluorescent Ultrashort Nanotubes 15
2.2.5 Length Characterization of Fluorescent Ultrashort Nanotubes 16
2.2.6 Control Experiment: Cutting Pristine SWCNTs in H_2O_2 17
2.2.7 Control Experiment: Piranha Solution Oxidation Cutting 18
2.2.8 NIR PL Imaging 18
2.2.9 Geometry Optimization and Natural Population Analysis 19
2.3 Results and Discussion 19
2.3.1 DICE Cuts Long Nanotubes into Ultrashort Pieces with Narrow Length Distribution 20
2.3.2 DICE Retains the Electric Structure of the Starting Nanotubes and Achieves High Yield 24
2.3.3 Bright PL from Ultrashort Nanotubes in the Shortwave Infrared 27
2.3.4 Alternative Defect Implanting Chemistry for DICE 33
2.3.5 Quantum Chemical Computation Suggests that DICE Follows Charge-Enhanced Reactivity at the Defect Site 34
2.4 Conclusions 36
Chapter 3: In-situ Spectroscopic Study Reveals Two-stage Defect-induced Chemical Cutting of Carbon Nanotubes 38
3.1 Introduction 38
3.2 Experimental Methods 38
3.2.1 Sorting purified (6,5) SWCNTs using ATPE Method 39
3.2.2 Functionalizing Pristine SWCNTs Using Diazonium Chemistry in Aqueous Solution 41

3.2.3 In-situ Monitoring the DICE Reaction 42
3.2.4 Control Experiment: DICE in Different Surfactants 42
3.3 Results and Discussion 43
3.3.1 Purified (6,5) Fluorescent Nanotubes with Controllable Defect Densities 43
3.3.2 Two-Stage Reaction Mechanism 45
3.4 Conclusions 48
Chapter 4: Summary and Outlook 50
4.1 Summary 50
4.2 Outlook for Fluorescent Ultrashort Nanotubes 51
4.2.1 Aqueous Solubility Enhancement through Structure Modifications 51
4.2.2 Potential Applications in Bioimaging and Sensing 52
Bibliography 53

List of Abbreviations

2D: Two-dimensional
AFM: Atomic force microscopy
AIBN: Azobisisobutyronitrile
ATPE: Aqueous two-phase extraction
D: Deuterium
DFT: Density functional theory
DICE: Defect-induced chemical etching
DNA: Deoxyribonucleic acid
DOC: Sodium deoxycholate
E_{11}: Excitonic transition between the first valence and conduction band van Hove singularities in a single-walled carbon nanotube
E_{11}^-: Quantum defect-induced electronic transition in single-walled carbon nanotube
E_{22}: Excitonic transition between the second valence and conduction band van Hove singularities in a single-walled carbon nanotube
E_{33}: Excitonic transition between the third valence and conduction band van Hove singularities in a single-walled carbon nanotube
f-SWCNT: Functionalized single-walled carbon nanotube
f+c-SWCNT: Functionalized and cut single-walled carbon nanotube
FT-IR: Fourier transform infrared
FUN: Fluorescent ultrashort nanotube
InGaAs: Indium gallium arsenide
NIR: Near infrared
NIR-II: Near infrared II
PEG: Polyethylene glycol
PL: Photoluminescence
RBMs: Radial breathing modes
RTC: Real-time-control
SC: Sodium cholate
SDS: Sodium dodecyl sulfate
SPE: Single-photon emission
SPS: Single-photon sources
SWCNT: Single-walled carbon nanotube
UV-VIS-NIR: Ultraviolet-visible-near infrared

Chapter 1: Fluorescent Ultrashort Nanotubes

1.1 Introduction to Single-Walled Carbon Nanotubes

A single-walled carbon nanotube (SWCNT) can be viewed as a molecular cylinder rolled-up from a graphene sheet with a specific wrapping vector defined by a pair of integers, (n, m) (Figure 1-1a). This vector, denoting the chirality of a SWCNT, determines its physical and chemical properties. SWCNTs are metallic for those with mod(n-m,3) = 0 and semiconducting with mod(n-m,3) = 1 or 2 (Figure 1-1b).[1] Metallic SWCNTs exhibit a continuum of energy levels, while semiconducting ones have a band gap between their valence and conduction bands, displaying an array of interesting electronic and optical properties.[2]

One of the most attractive optical characteristics of semiconducting SWCNTs is direct band-gap photoluminescence (PL). An electron in the valence band can be excited to the conduction band with light, leaving a hole in the valence band. In SWCNTs, the electron-hole pair is strongly bound by Columbic interactions and behaves like a quasi-particle called exciton. The exciton can relax radiatively through E_{11} PL when the electron and hole recombine (Figure 1-1c).[3]

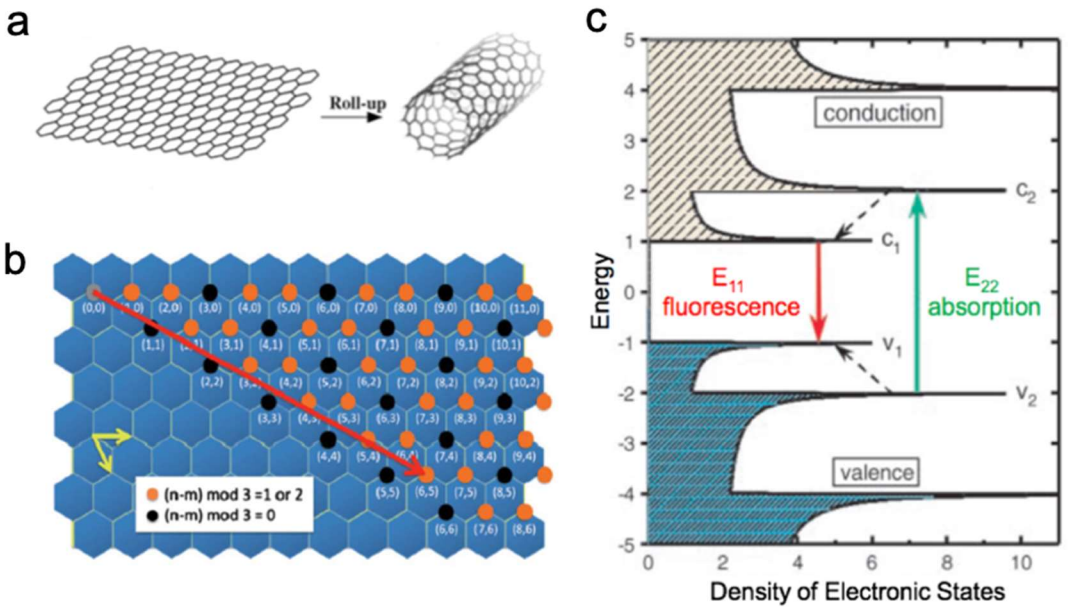

Figure 1-1. (a) Schematic of a SWCNT rolled-up from a graphene sheet. (b) Schematic of graphene with wrapping vectors for a SWCNT. (c) Density of electronic states for a semiconducting SWCNT. Dashed arrows describe non-radiative relaxation pathways. Figures adapted from reference.[1-3]

1.2 Fluorescent Ultrashort Nanotubes: Potentials and Significance

Ultrashort SWCNTs that fluoresce brightly in the shortwave infrared have been a long sought-after synthetic target.[4-10] The strong motivations behind this pursuit also include understanding of quantum confinement along the nanotube length,[6, 11, 12] as well as the potential use of this family of carbon semiconductors in bio-imaging, bio-sensing and single photon source applications.[13-18]

1.2.1 Biocompatible Emitters in Bioimaging and Sensing

The PL of SWCNTs makes them attractive candidates for bio-imaging and bio-sensing. In particular, the PL of SWCNTs is located in the near infrared II (NIR-II

window, 1000-1700 nm), which can penetrate biological tissues up to centimeters depth and achieves micrometer-scale resolution at depths of millimeter because of low scattering and absorption by tissues in this range. Additionally, tissue autofluorescence is very weak in this window, reducing background noise in bio-imaging.[13] It has been reported that fluorescent SWCNTs allowed deep and sensitive *in vivo* imaging of blood vessels beneath and through the deep layers of skin.[14] *In vivo* near infrared (NIR) imaging of tumors was also achieved by using SWCNTs as photoluminescent probes.[17] Selective detection of nitric oxide, which plays a significant role in the regulation of pulmonary vasomotor tone[19] in mice lung tissue, was also achieved using SWCNTs as *in vivo* photoluminescent biosensors.[18]

The promise of SWCNTs in bio-imaging and bio-sensing, however, has been severely limited by toxicity and biocompatibility concerns.[13, 14, 20-22] Many experiments suggest that the biotoxicity of SWCNTs can be addressed by decreasing the length of the materials to ultrashort scales (< 80 nm).[20, 22] For example, Kostarelos showed that short nanotubes (< 1000 nm) do not react with the mesothelium of the lungs, thus preventing inflammation and granuloma in mice.[22] Moussa and colleagues also reported that well-individualized and sufficiently short (< 300 nm) SWCNTs can be eliminated through the kidney and bile ducts, and suggested that discrete, individual "molecule-like" ultrashort nanotubes are the key for achieving the promise of SWCNTs in bio-imaging.[20] In addition to the increased biocompatibility, ultrashort nanotubes promise to significantly improve imaging resolution in the shortwave infrared due to their exceptionally small sizes.

Considering their fluorescence in the NIR-II window and low biotoxicity, fluorescent ultrashort nanotubes therefore become ideal emitters in the bioimaging and sensing applications.

1.2.2 Efficient Single-Photon Sources

Single-photon sources (SPSs) operated at room temperature and telecommunication wavelengths (1260-1625 nm) show great potentials as quantum light sources for quantum computing and cryptography.[23] The photo antibunching property enables SWCNTs to become promising candidates.[24] Single-photon emission (SPE) from pristine air-suspended SWCNTs exhibit high quantum efficiency but low purity (< 80%, $g^2(0) > 0.2$).[25] The localization of excitons at the defect enables high purity SPE ($g^2(0)$ ~0.01) from unsuspended SWCNTs. However, the single-photon generation efficiency is still low (13%).[9, 23, 26]

Recently, Hideyuki Maki et al. theoretically predict that both single-photon purity and generation efficiency can be simultaneously achieved by shortening and functionalizing air-suspended SWCNTs.[27] Based on a Monte Carlo simulation, ultrashort (100 nm) air-suspended functionalized (with an aryl group) SWCNTs under high excitation conditions show single-photon purity of 99.87% and single-photon generation efficiency of 99.84%. However, limited by the synthetic challenge, this prediction has yet to be verified by any experiments.

1.3 Fluorescent Quantum Defects Enable Ultrashort Nanotubes to Fluoresce

Despite the great promise of fluorescent ultrashort nanotubes, ultrashort SWCNTs typically do not fluoresce. The diminishing of PL is due to the short length

of nanotubes. When the exciton (electron-hole pair) is diffusing along the nanotubes, the electron and hole may radiatively recombine to emit a photon. However, this occurs efficiently only when the diffusion length of exciton—the maximum distance that an exciton can travel within its lifetime—is smaller than the nanotube length. When the nanotube length becomes less than this threshold (~100-240 nm),[28, 29] most excitons will encounter the nanotube ends before they can radiatively recombine.[9, 10, 30] Unfortunately, these nanotube ends usually behave as quenching sites, causing the loss of the SWCNT PL (Figure 1-2a).[9] Due to the PL quenching in short nanotubes, their applications remain largely underexplored.

Our recent work demonstrates that intense PL can in fact be generated in ultrashort nanotubes (~40 nm) through the incorporation of fluorescent sp^3-defect sites.[9] In that study (Figure 1-2b, c), we were able to produce a small sample of ultrashort nanotubes that were fluorescent using SWCNTs that had been broken into smaller segments by ultrasonication and then functionalized with perfluorinated hexyl functional groups ($-C_6F_{13}$). Super-resolution PL imaging suggests that the implanted $-C_6F_{13}$ groups preferentially locate at the nanotube ends and can trap excitons, preventing them from encountering other end-defects that typically act as quenching sites. Trapping at these optically allowed defect sites allows the excitons to radiatively recombine, generating a defect-induced PL peak that is redshifted from the native nanotube PL.[26, 31, 32]

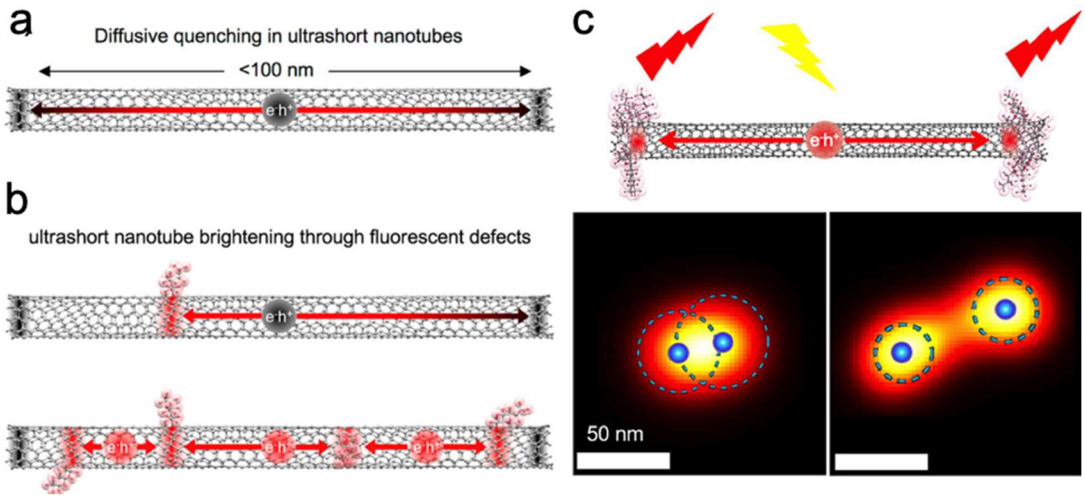

Figure 1-2. (a) Schematic of excitons diffusing along pristine ultrashort SWCNTs. Excitons encounter quenching defects located on nanotube ends and PL is quenched. (b) Schematic of excitons diffusing along functionalized ultrashort SWCNTs. Implanted defects can trap excitons and generate bright PL. (c) Super localization resolves defects and demonstrates that fluorescent quantum defects are preferentially located on both ends of nanotubes. Defects are separated by less than 40 nm. Figures adapted from reference.[9]

1.4 Synthesis of Ultrashort Nanotubes

Existing approaches to synthesizing ultrashort nanotubes are top-down strategies, i.e., long carbon nanotubes are cut into shorter segments. Current nanotube-cutting techniques include mechanical methods that rely on mechanical strength to break the nanotubes,[8, 33] and oxidation methods that use strong oxidants to react and etch carbon atoms.[4, 34, 35]

1.4.1 Mechanical Cutting: Tip Sonication

Mechanical cutting, such as tip sonication is widely used to disperse carbon nanotubes in aqueous solution, as well as shorten the nanotubes. Poulin et al. systematically studied the kinetics of nanotube scission under sonication.[36] Gas bubbles

are generated by acoustic waves in liquid first, and then grow through rectified diffusion and coalescence. When reaching the critical size, the gas bubbles collapse, generating a strong flow field in the surrounding liquid. As illustrated in Figure 1-3a, in the existence of the flow field, carbon nanotubes align radially, and in this orientation, fluid flows faster around the end near the tip than the other end of the nanotube. This flow rate difference results in an intense drag force that may break the nanotube. Experimentally, it is found that the mean nanotube length L decreases with sonication time and power (Figure 1-3b) and L correlates with the acoustic energy (Figure 1-3c) by $L \sim E^{-0.22}$. Noy et al. reported the synthesis of ultrashort nanotubes (10 - 20 nm) using intense (17 – 19 W) and long time (16 h) ultrasonication, and fabricated nanotube porins for the study of ion transport in single digit nanopores.[37] However, sonication usually results in a broad length distribution and low yield of the cut nanotubes.[6, 10]

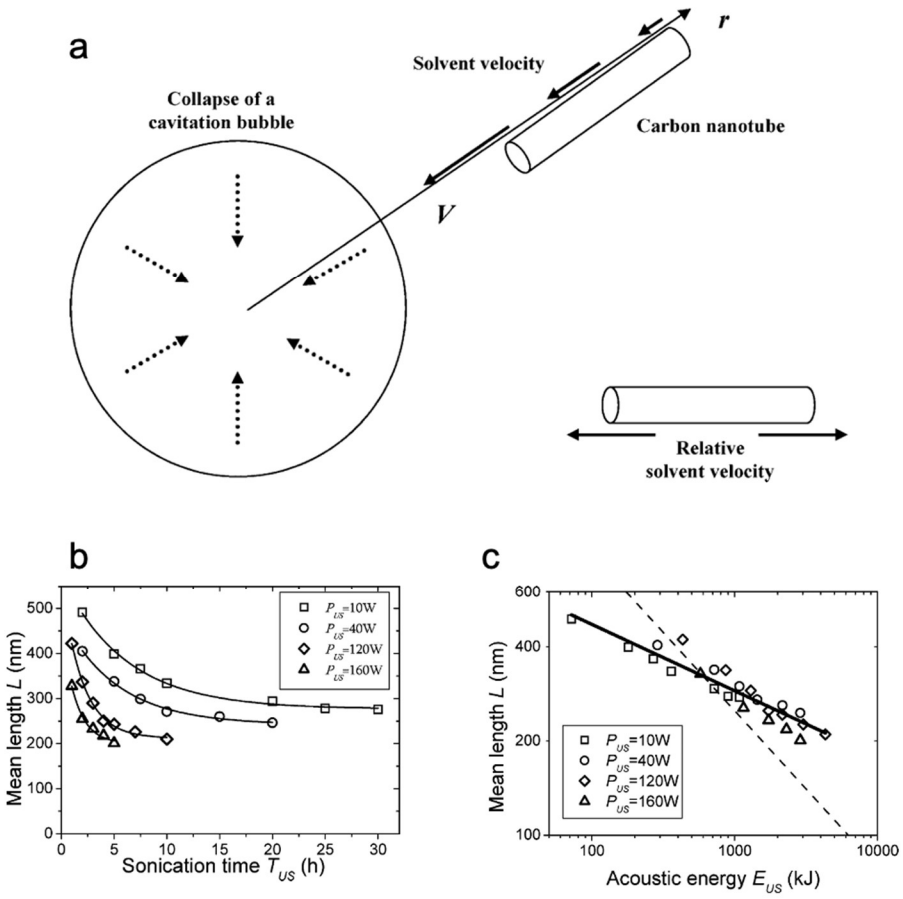

Figure 1-3. (a) Scheme of a nanotube near a cavitation bubble in ultrasonication; Average length of nanotubes as a function of (b) sonication time and (c) for the acoustic energy for different sonication powers. Figures adapted from reference.[36]

1.4.2 Chemical Cutting: Oxidative Cutting

Chemical cutting methods are also well developed in which strong oxidants are commonly used to cut the nanotubes. For instance, Ziegler et al. reported a controlled oxidative cutting of SWCNTs using piranha solution (96% H_2SO_4 + 30% H_2O_2, *v/v* = 4:1) and explored how temperature will affect the reaction (Figure 1-4).[34] At high temperature (70 °C), piranha was found to generate new vacancies on the nanotube

sidewalls, and then consume the oxidized vacancies and existing damage sites, cutting the nanotubes short. The mean length of carbon nanotubes decreases as oxidation time increases. At room temperature (22 °C), however, piranha typically do not generate new vacancies, the cutting occurs at existing damage sites in a controllable manner, and therefore exhibits slower etching rate, minimal carbon loss and little sidewall damage.

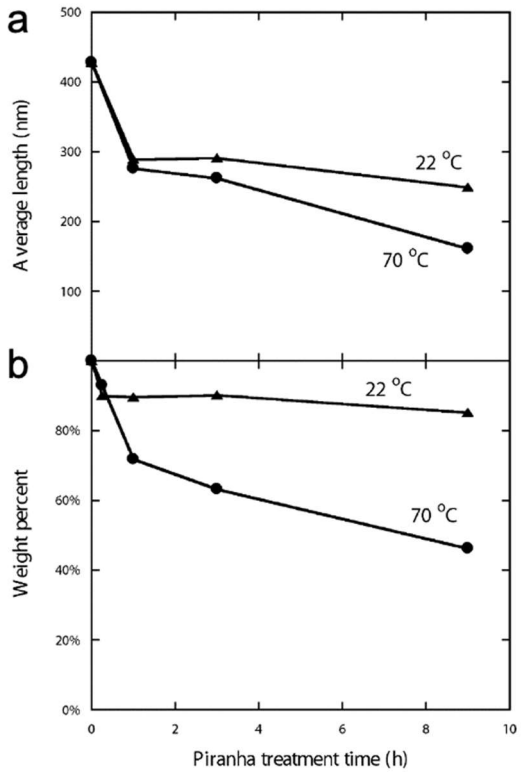

Figure 1-4. (a) Average nanotube length and (b) weight loss as a function of piranha treatment time for reactions at 22 °C and 70 °C. Figures adapted from reference.[34]

A mixture of 98% H_2SO_4 and 70% HNO_3 (*v/v* = 3:1) is also demonstrated to effectively yield short nanotubes. Intensive sonication in this acid mixture at low temperature (< 8 °C) for 30 h can shorten nanotubes length from 1-2 μm to 50-200 nm with minimal carbon loss.[35]

All cutting strategies introduced above are capable of yielding ultrashort nanotube; however, none of them are capable of synthesizing ultrashort nanotubes that fluoresce brightly in the shortwave infrared. It was believed that fierce oxidation severely damages the nanotube sidewalls, causing the loss of nanotube PL properties.[34, 38]

1.5 Synthetic Challenges Addressed in this Thesis

Ultrashort nanotubes are proven capable of fluorescing by implanting fluorescent quantum defects,[9] but the sonication-based approach to the synthesis suffers from long processing time (pulsed tip sonication at 45 W for 10 h and ultracentrifugation for 2 h), microscopic scale, and low yields (< 10%). These limitations make it challenging to produce adequate samples for many experiments, such as biological imaging, where high-dose injection into live animals is usually required.[39] In this thesis, I aim to solve this synthetic challenge and to develop a facile and efficient method that can produce fluorescent ultrashort nanotubes in a scalable manner.

In Chapter 2 of this thesis, we will introduce a defect-induced chemical cutting method. The synthesis and properties of fluorescent ultrashort nanotube (FUNs) will also be studied based on spectroscopic characterization, length distribution analysis and explored the reaction mechanism using quantum computing.

Chapter 3 will elucidate the detailed molecular mechanism of defect-induced chemical etching of nanocarbon. The defect PL and nanotube absorption properties make it possible for us to follow the defect-induced chemical etching (DICE) process

by in-situ spectroscopy. Our results reveal a cut-then-etch two-step mechanism, suggesting a neat approach to synthesize FUNs with extraordinary controls.

Finally, I will summarize the key results presented in this thesis and provide an outlook of the potential applications and new experiments with FUNs.

Chapter 2: Synthesizing Fluorescent Ultrashort Nanotubes from Defect-Induced Chemical Cutting

Adapted from the manuscript: Li, Y.; Wu, X.; Kim, M.; Fortner, J.; Qu, H.; Wang, Y., Fluorescent Ultrashort Nanotubes from Defect-Induced Chemical Cutting. *Chemistry of Materials* **2019,** *31* (12), 4536-4544.

Contributions note: Li, Y. conceived the defect-induced chemical cutting methodology, conducted spectroscopic and length characterization of fluorecent ultrashort nanotubes, and drafted the manuscript.

2.1 Introduction

Ultrashort SWCNTs that fluoresce brightly in the shortwave infrared could open exciting opportunities in high-resolution bio-imaging and sensing. However, this material remains largely unexplored due to the synthetic challenge. To solve this synthetic challenge and address the associated fundamental questions concerning the roles of defects in oxidative chemistry, herein we demonstrate a defect-induced chemical etching strategy (Figure 2-1) that enables a scalable synthesis of fluorescent ultrashort nanotubes. DICE is a straightforward, two-step process that involves first covalently implanting *p*-nitroaryl defects on the SWCNT sidewalls through diazonium chemistry and then cutting the nanotubes by hydrogen peroxide (H_2O_2). In the first step, the implanted *p*-nitroaryl defects not only provide preferential cutting sites for H_2O_2 and thus accelerate the cutting process, but also generate a defect-induced emission peak (E_{11}^-),[9, 26, 31] which is redshifted from the nanotube's intrinsic E_{11} PL, allowing us to use it as an optical fingerprint to track this reaction. In the second step, H_2O_2 selectively cuts the nanotubes from the implanted defect sites without introducing

additional sidewall defects. Quantum chemical computations reveal that the *p*-nitroaryl groups introduce negatively charged, reactive sp^3-defect centers on the nanotube sp^2 lattice where H_2O_2 oxidation preferentially occurs. With this defect selective chemistry, we were able to synthesize FUNs with a narrow length distribution (38 ± 18 nm) at a yield as high as 57% while simultaneously generating bright PL in the shortwave infrared. Our work thus lays the foundation for the scalable synthesis of FUNs, enabling further studies of this new material and their potential incorporation in bio-imaging and bio-sensing applications.

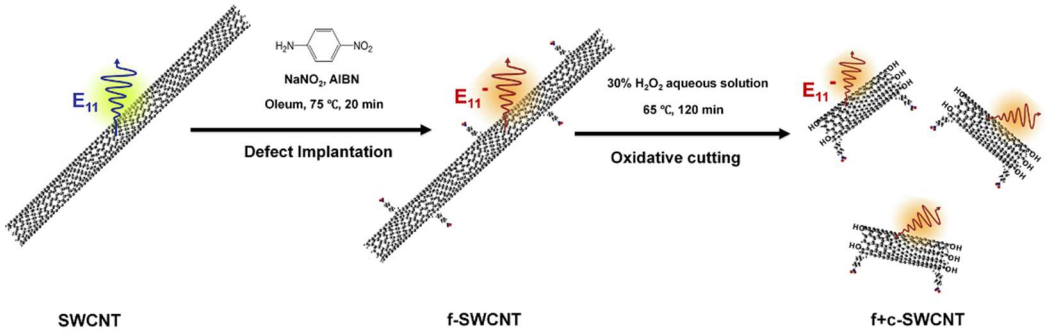

Figure 2-1. Schematic of DICE. This functionalize-then-cut two-step process involves (1) implanting sp^3 chemical defects along the SWCNT sidewalls by covalently attaching organic functional groups (e.g., *p*-nitroaryl as illustrated here) to form f-SWCNTs, and then (2) cutting the f-SWCNTs with H_2O_2 into ultrashort nanotubes (f+c-SWCNTs) that fluoresce in the shortwave infrared. Note that E_{11} emission is the intrinsic PL of the SWCNT while E_{11}^- emission is the defect-induced PL in the f-SWCNT and f+c-SWCNT.

2.2 Experimental Methods

2.2.1 Implanting sp^3 Defects in SWCNTs

The first step of DICE is the functionalization of SWCNTs with sp^3 quantum defects. Raw CoMoCAT SG65i SWCNTs (≥ 99%, Lot No. SG65i-L39, SouthWest NanoTechnologies; 6 mg) were added to oleum (20% free SO_3, Sigma-Aldrich; 20 mL) and stirred to ensure the nanotubes were well dispersed. *Safety note: the functionalization reaction must be performed in a fume hood. Protective gloves and masks are needed when transferring oleum, which is extremely acidic and corrosive.* $NaNO_2$ (Analytical standard, Sigma-Aldrich; 1.725 mg) and *p*-nitroaniline (Analytical standard, Sigma-Aldrich; 3.45 mg) were then added to the system, keeping the molar ratio of carbon atoms to *p*-nitroaryl groups at 20:1. The system was heated to 75 °C, and then 5.0 mg of azobisisobutyronitrile (AIBN, 98%, Sigma-Aldrich) was added as a radical initiator. After 20 min heating and stirring, the system was removed from the hot plate. After cooling down, the oleum solution was carefully transferred to 500 mL of 2.0 M NaOH (≥ 97%, Sigma-Aldrich) aqueous solution, drop by drop, to neutralize the ultra-concentrated sulfuric acid until the system reached pH 8. *Note that this neutralization step is exothermic and can produce corrosive fumes and therefore it must be done slowly in a fume hood.* We then vacuum-filtrated the solution to collect the functionalized single-walled carbon nanotube (f-SWCNTs), followed by rinsing the material with water and ethanol several times to remove impurities. The f-SWCNTs obtained on filter paper were dried in vacuum for 1 h.

2.2.2 Cutting f-SWCNTs in H_2O_2

The second step of DICE is cutting f-SWCNTs in H_2O_2. 2 mg of f-SWCNTs were homogenized in 10 mL of deionized water (milli-Q water) with 1 wt% sodium deoxycholate (≥ 98%, DOC, Sigma-Aldrich) by bath sonication for 30 min. 10 mL of H_2O_2 (30 wt% in H_2O, Sigma-Aldrich) was then added and mixed well with the SWCNT surfactant dispersion. The solution was then heated to 65 ℃ using an oil bath while magnetically stirred until the SWCNTs were totally digested and the solution became transparent. Functionalized and cut single-walled carbon nanotube (f+c-SWCNT) samples were collected every 30 min for characterization. Four fractions of samples were collected at 30 min, 60 min, 90 min, and 120 min. *Safety note: H_2O_2 aqueous solution is oxidative and corrosive; avoid exposure to skin and eyes.*

2.2.3 Alternative Approach of Defect Implanting for DICE

We dispersed 1.0 mg of raw CoMoCAT SG65i SWCNTs in 10 mL of D_2O (99.8 atom % D, Cambridge Isotope Laboratories, Inc.) with 1 wt% sodium dodecyl sulfate (SDS, Sigma-Aldrich) by tip sonication at 4 W for 30 min. We then diluted the stock solution using D_2O until the (6,5) nanotube optical density at E_{11} equals 0.364. 7.72 mg of 4-nitrobezenediazounium tetrafluoroborate powder (Sigma-Aldrich, 97%) was dissolved in 1 mL of D_2O, followed by a serial dilution (dilution factor = 1:1000). We added 250 μL of this diluted solution to 2 μL of the dispersed SWCNTs in SDS/D_2O solution in a cuvette, and then illuminated the solution with 565 nm light using a NanoLog spectrofluorometer (Horiba Jobin Yvon) while stirring the sample using a magnetic bar. We monitored the reaction in real-time-control (RTC) mode and

terminated the reaction by turning off the laser when the E_{11}^- peak (~1150 nm) became stable. This process was repeated 5 times to prepare ~10 mL solution of f-SWCNTs.

We then added 5 mL of H_2O_2 (30 wt% in H_2O) to 5 mL of the prepared f-SWCNTs in SDS/D_2O solution. The solution was then heated to 65 ℃ using an oil bath while being magnetically stirred. The resulting f+c-SWCNT samples were collected after 2 h of oxidative cutting with H_2O_2.

2.2.4 Spectroscopic Characterization of Fluorescent Ultrashort Nanotubes

UV-VIS-NIR absorption spectra were collected by a spectrophotometer with a broadband InGaAs detector (Lambda 1050, PerkinElmer). To calculate the yield, f-SWCNTs before and after oxidation were dispersed in 4 mL of 1 wt% DOC in H_2O.

The PL spectra and 2D excitation-emission PL map were collected on the NanoLog spectrofluorometer. To exclude effects of H_2O_2 on the PL, we added 8 μL of 8 mg $Na_2S_2O_4$ (technical grade, Sigma-Aldrich) / 0.1 mL of D_2O solution to quench residual H_2O_2, followed by adding a few microliters of 8 mg $NaHCO_3$ (≥ 99.7%, Sigma-Aldrich) / 0.1 mL of D_2O aqueous solution until the system was weakly basic (pH ~8). The samples were excited with a 450 W Xenon source dispersed by a double-grating monochromator. The slit width of the excitation and emission beams were 10 nm. The PL spectra were collected using a liquid-N_2 cooled linear InGaAs array detector. Note that all samples had an optical density at the E_{11} band of 0.10. The integration time for the PL spectra and 2D map were 2 s and 5 s, respectively. Samples were diluted in D_2O to avoid the absorption of H_2O at ~1200 nm.

Raman spectra were recorded from 150 to 3000 cm^{-1} using a LabRAM ARAMIS Raman microscope (Horiba Jobin Yvon) with a 633 nm excitation. The

integration time was 0.8 s, taken 10 times in total. The power density of the incident laser was 1.2 $mW/\mu m^2$.

Fourier transform infrared (FT-IR) spectra of both pristine SWCNTs and f+c-SWCNTs (120 min H_2O_2 oxidation) were collected using a Thermal Nicolet NEXUS 670 FT-IR with an attenuated total reflection attachment.

2.2.5 Length Characterization of Fluorescent Ultrashort Nanotubes

We use atomic force microscopy (AFM) to analyze the length of nanotubes. For AFM characterization, we drop-cast the SWCNT solutions on freshly cleaved mica surfaces and allowed the droplet to remain on the substrate for 5 min, after which it was blown off using air. Then the substrate was gently rinsed with water and ethanol in sequence to remove surfactant and other impurities, followed by blowing the sample dry with air. We imaged the substrate using AFM probes with a tip radius of less than 5 nm (TAP 300GD-G AFM Probe from BudgetSensors) in the AC-air mode of an Asylum Cypher ES AFM system. We obtained topography images at a sampling rate of 0.8 Hz and a 512-line resolution. We measured more than 100 nanotubes for each sample to analyze the length distributions using Gwyddion software. The nanotube length follows the normal distribution and we report the distributions as $\mu \pm \sigma$ in the discussions where μ is the mean and σ the standard deviation. In the correlated study of the AFM and PL images in the same region of interest, we used the same method to prepare the sample, though the substrate was changed to a polystyrene-Au-Si wafer substrate for PL imaging. We located the same region of the sample for correlated AFM/PL analysis using fluorescent markers on the substrate.

2.2.6 Control Experiment: Cutting Pristine SWCNTs in H_2O_2

In order to study the effect of implanted defects on oxidation, we compared the cutting efficiency of f-SWCNTs by applying the same cutting strategy to pristine SWCNTs. 2 mg of CoMoCAT SG65i SWCNTs were homogenized in 10 mL of 1 wt% DOC/H_2O by bath sonication for 30 min. 10 mL of 30% H_2O_2 was then added and mixed well with the SWCNT solution, followed by heating at 65° C while stirring. We collected the cut pristine nanotubes after 2 h and analyzed the AFM height images. We also collected the cut pristine nanotubes after 2 h, 4 h, 6 h and 8 h oxidation, and measured the 2D excitation-emission PL map of these samples with integration times of 1 s.

2.2.7 Control Experiment: Piranha Solution Oxidation Cutting

2 mg of dry f-SWCNT powder was collected and well-dispersed in 2 mL of oleum. 10 mL of piranha solution (98% H_2SO_4 + 30% H_2O_2, *v/v* = 3:1) was then prepared with caution in an ice bath. We added the f-SWCNT/oleum solution slowly to the piranha solution in a 30 mL vial. The solution was heated up to 65 ℃ on a hot plate and magnetically stirred. After 30 min oxidation, we removed the vial from the heat source and neutralized the solution by slowly adding it to an excess amount of NaOH aqueous solution (2.5 M), followed by filtering the oxidized f-SWCNTs. *Note that piranha solution and oleum are highly oxidative and acidic, protective gloves and masks are required, and skin and eye contact should be avoided.*

2.2.8 NIR PL Imaging

5 µl of the f+c-SWCNT solution was spread and then dried on a polystyrene coated Au-on-Si wafer substrate. The ultrashort nanotubes were imaged with a custom-built shortwave infrared imaging system using an IR optimized objective (Olympus LCPLN100XIR, NA 0.85) and a liquid nitrogen cooled InGaAs detector (Cougar-640-LN2, Xenics, Belgium). The sample was excited with a 730 nm laser at intensities kept below 64 W/cm^2 to avoid nonlinear effects. Note that this off-resonant excitation generates E_{11} excitons in (6,5)-SWCNTs and does not directly excite the emissive defects. To obtain the locations of emissive defects, we recorded a 10 min image sequence of the blinking defect emission by placing a 1100 nm long-pass filter before the InGaAs detector. The image sequence was analyzed to retrieve the super-resolved defect locations as we previously reported.[9, 40]

2.2.9 Geometry Optimization and Natural Population Analysis

The density functional theory (DFT) calculations were performed using Gaussian 09 software.[41] We used a 4 nm long (6,5)-SWCNT with open ends terminated by hydrogens. To model a f-SWCNT, we introduced a *p*-nitroaryl paired with a hydrogen group in the middle of the (6,5)-SWCNT. Geometry optimization was performed with the B3LYP functional and 3-21G basis set. The B3LYP functional is widely used to predict the electronic and optical properties of large organic molecules. For f+c-SWCNTs where aryl defects are covalently bound to the nanotube, B3LYP produces results that are qualitatively consistent with calculations made using larger a DFT functional because the orbital localization properties are much less sensitive to the long-range corrections. The 3-21G level of theory is suitable to obtain the optimized

geometries of the covalently functionalized nanotube systems and their electronic structures. To determine the partial atomic charges, we performed Natural Population Analysis[42] on the geometrically optimized model using the NBO 3.1 software included in Gaussian 09. As the charges found from Natural Population Analysis should converge as the basis set quality increases, we also performed the DFT optimization at the B3LYP/6-31G level to show that using a larger basis set has minimal effect on the calculated charges (Figure 2-12).

2.3 Results and Discussion

Our DICE strategy begins by covalently implanting *p*-nitroaryl groups on the sidewalls of pristine, long SWCNTs. This step can be achieved using diazonium chemistry in oleum,[43] although this step should be achievable with other chemistries.[31, 44] Then we homogenize these f-SWCNTs in 1 wt% DOC/H_2O, followed by adding H_2O_2 and heating at 65 °C to cut the nanotubes by chemical oxidation. H_2O_2 is unstable at this temperature and spontaneously decomposes to hydroxyl and hydroperoxyl radicals, which can oxidize nanotube carbon.[45, 46] We hypothesized that these free radicals would selectively oxidize the more reactive sp^3 defect sites implanted at the first step of the synthesis to cut the long f-SWCNTs into shorter pieces, and this hypothesis is supported by both our experimental results and quantum chemical simulations, which will be discussed later. After this two-step functionalize-then-cut process, we obtain ultrashort nanotubes with implanted *p*-nitroaryl defects that emit at ~1150 nm, characteristic of the *p*-nitroaryl defects.[9, 26, 31]

2.3.1 DICE Cuts Long Nanotubes into Ultrashort Pieces with Narrow Length Distribution

We first investigated the effect of the H_2O_2 oxidation time on the length distribution of the f+c-SWCNTs by collecting a sample from the reaction every 30 min and characterizing it using AFM. Figure 2-2a-d show representative height images of the f+c-SWCNTs made with varying oxidation times. We randomly sampled > 100 nanotubes from each fraction and plotted a stacked 2D histogram of the SWCNT length distribution in Figure 2-2e. Without oxidation, the f-SWCNTs featured a normal length distribution of 197 ± 106 nm. Meanwhile, f+c-SWCNT samples with oxidation times of 30 min, 60 min, 90 min, and 120 min showed normal length distributions of 112 ± 69 nm, 70 ± 44 nm, 60 ± 31 nm, and 38 ± 18 nm, respectively, in which we observed decreasing average length and narrowing size range with increased oxidation time. The system began with a disordered mixture of long and short nanotubes, but after 120 min ended with only ultrashort nanotubes that featured a narrow distribution of lengths.

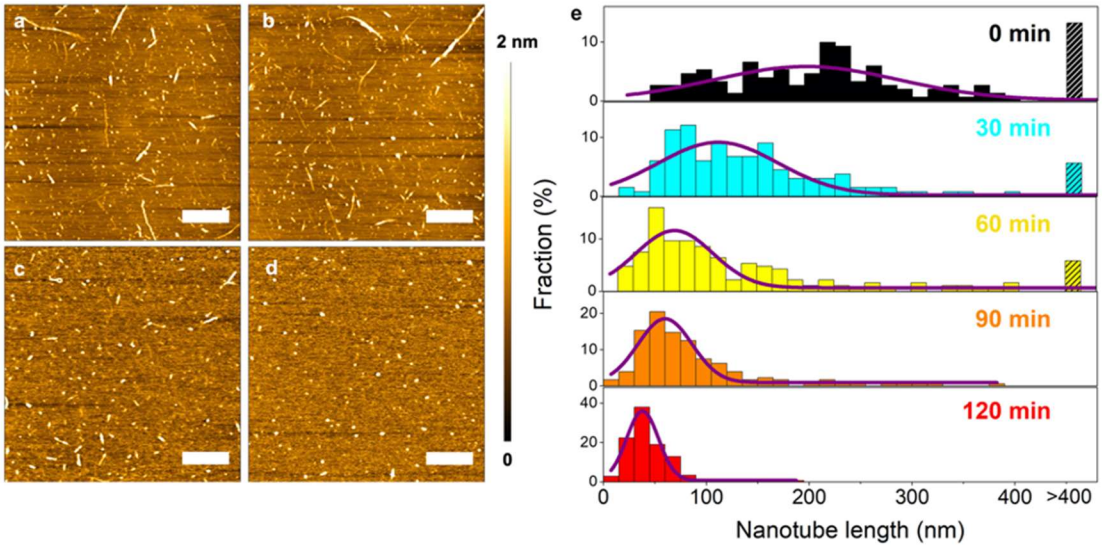

Figure 2-2. DICE cuts long nanotubes into ultrashort pieces with a narrow distribution of lengths. Representative AFM height images of f+c-SWCNTs with different

oxidation times: (a) 30 min, (b) 60 min, (c) 90 min, and (d) 120 min. The nanotubes were deposited on mica surfaces. Scale bars: 1 μm. (e) Histograms of the length distributions of f-SWCNTs (0 min) and f+c-SWCNTs after 30, 60, 90, and 120 min oxidation. Lengths larger than 400 nm were combined into one bin (dark slashed bar).

Our DICE strategy is significantly more efficient at producing ultrashort nanotubes compared to the tip sonication method.[8, 33] While 2 h tip sonication at 4 W shortened the average length of the f-SWCNTs from 197 nm to 137 nm (Figure 2-3), DICE produced f+c-SWCNTs that were 38 ± 18 nm in length for the same processing time (Figure 2-2d-e). Additionally, the tip sonicated sample contained a considerable fraction of long nanotubes (> 200 nm: ~38%, Figure 2-3d), but none were observed in the DICE sample. Clearly, our DICE strategy produces shorter nanotubes with a much narrower length distribution.

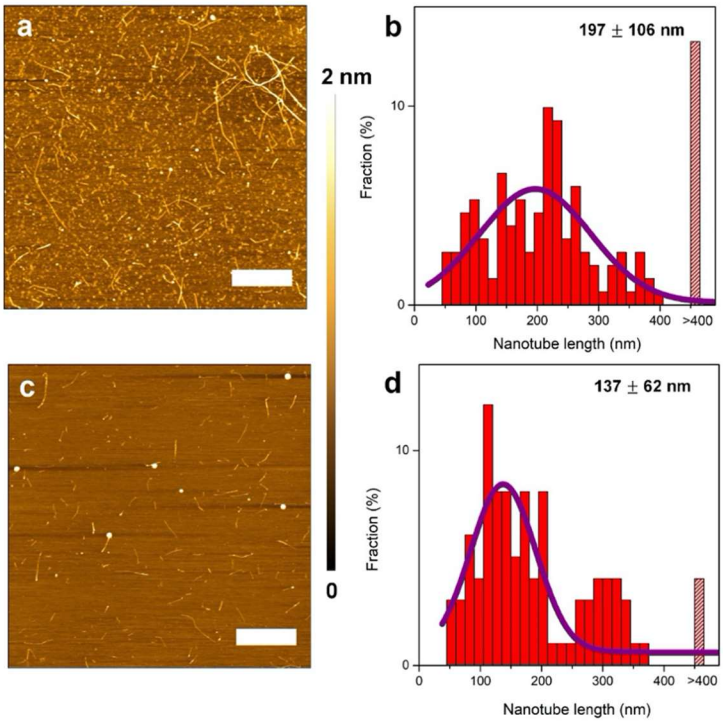

Figure 2-3. AFM characterization of the cutting efficiency of the conventional tip sonication method. (a) AFM image and (b) length distribution histogram of the f-SWCNTs before tip sonication. (c) AFM image and (d) length distribution histogram of f-SWCNTs cut by tip sonication at 4 W for 2 h. Scale bars: 1 μm. In both length distribution histograms, lengths larger than 400 nm were combined into one bin (slashed bar).

An important observation from DICE is that the *p*-nitroaryl defects accelerate the oxidative cutting of f-SWCNTs. We performed the same cutting experiment with pristine nanotubes as a control (see the Experimental Section for details). After 2 h oxidation, for the non-functionalized control the nanotubes were shortened from 193 ± 98 nm to just 119 ± 81 nm, and a large portion of the long nanotubes remained (> 200 nm: ~30%, Figure 2-4). This is in stark contrast with the f+c-SWCNTs, which achieved a length distribution of 38 ± 18 nm (Figure 2-2e) after the same 2 h oxidation, with nearly all nanotubes converted into ultrashort materials. This acceleration effect supports our hypothesis that the oxidation reaction selectively occurs from more reactive defect sites. In pristine nanotubes, H_2O_2 only etches from the nanotube ends,[44] while in f-SWCNTs, our results suggest that oxidation preferentially cuts the nanotubes into shorter pieces at the defect sites.

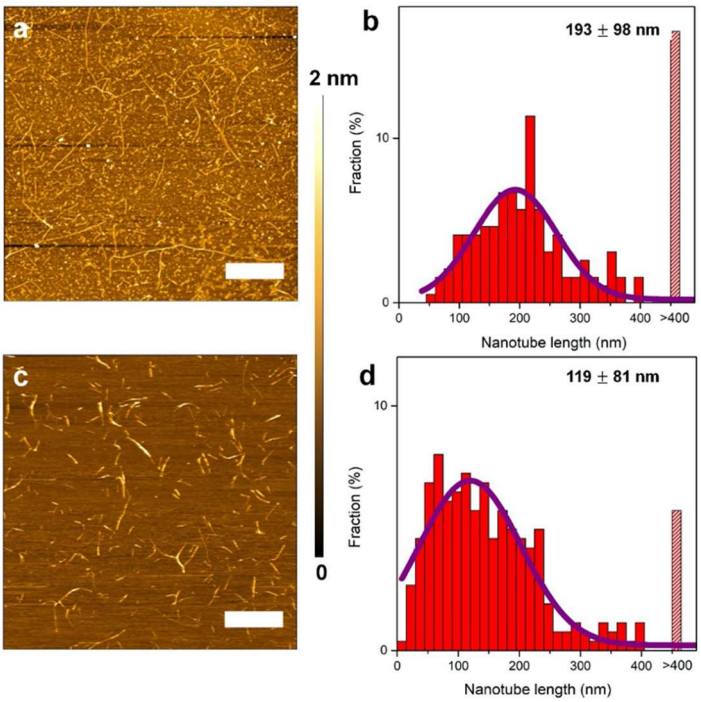

Figure 2-4. A control for the acceleration effect in the oxidation process due to defect implantation. (a) AFM image and (b) length distribution histogram of pristine SWCNTs before H_2O_2 oxidation. (c) AFM image and (d) length distribution histogram of pristine SWCNTs after 2 h H_2O_2 oxidation. This control experiment was performed under the same experimental conditions as that of Figure 2-2. Scale bars: 1 μm. In both length distribution histograms, lengths larger than 400 nm were combined into one bin (slashed bar).

2.3.2 DICE Retains the Electric Structure of the Starting Nanotubes and Achieves High Yield

The electrical and optical properties of SWCNTs are substantially affected by defects or functional groups,[47, 48] so it is critical to keep the nanotube graphitic structure intact as much as possible during the oxidation process. Figure 2-5a shows the Raman spectra of the f+c-SWCNTs with different oxidation times. The results show that the integrity of the nanotube radial breathing modes (RBMs) are not affected by the cutting

process, suggesting that the basic nanotube structure remains undamaged during exposure to H_2O_2. The G peak located at ~1580 cm^{-1} arises from the stretching of the sp^2 C-C bonds in graphitic materials and the D peak located at ~1310 cm^{-1} is caused by the presence of disorder (i.e., sp^3 carbon), with the ratio of the D/G peaks being conventionally used to quantify the SWCNT structural integrity.[49] Figure 2-5b summarizes the change of the D/G ratio of the f+c-SWCNTs as a function of oxidation time. The D/G ratio remains very low and constant (~0.05) even with prolonged oxidation, indicating no increase in the total number of defects as a result of H_2O_2 cutting. These results agree with the cutting mechanism we have proposed, in which H_2O_2 cuts f-SWCNTs selectively from the defect sites, leaving oxygen-containing groups on the ends of the f+c-SWCNTs, while introducing no sidewall damage during cutting.

We also investigated oxidative cutting of f-SWCNTs using piranha solution (see the Experimental Section for details). Piranha solution also cuts the f-SWCNTs, but the chemical reaction severely damages the nanotube electronic structure. In Figure 2-5a-b, we observed a significant increase of the D/G ratio from 0.05 to 0.25 and the deformation of the RBMs after applying piranha solution to the same f-SWCNTs. This is consistent with previous work by Ziegler et al., which showed that the Piranha reaction introduces a large number of oxygen-containing defects as well as vacancies along the nanotube sidewalls,[50] resulting in the loss of the SWCNT electronic structure and thus quenching the PL in these samples. In our case, the loss of both the E_{11} and E_{11}^- PL unambiguously confirms that the piranha reaction is so aggressive that the defect PL does not survive. In contrast, H_2O_2 enables controllable cutting, which is

critical for keeping both the electronic structure of the nanotubes and the aryl functional groups intact.[34]

Importantly, DICE achieves a high yield in synthesizing FUNs from SWCNTs. In Figure 2-5c, we compared the f-SWCNT solution before and after 120 min H_2O_2 oxidation. The color of the solution becomes lighter after DICE due to carbon consumption during the etching process. To determine the yield, we measured the UV-VIS-NIR absorption spectra of the samples before and after oxidation (Figure 2-5d). Because the absorbance of (6,5) SWCNT is proportional to the number of carbon atoms,[12, 51] the yield of DICE can be evaluated from changes in the E_{11} absorption band,41-42 and we obtained a yield as high as 57% for converting SWCNTs into FUNs. It is worth noting that the E_{11} absorption peak blue-shifted 18.8 meV after 120 min oxidative cutting, which may be attributed to the quantum confinement of E_{11} excitons due to the reduced nanotube size.[7, 8, 11, 52]

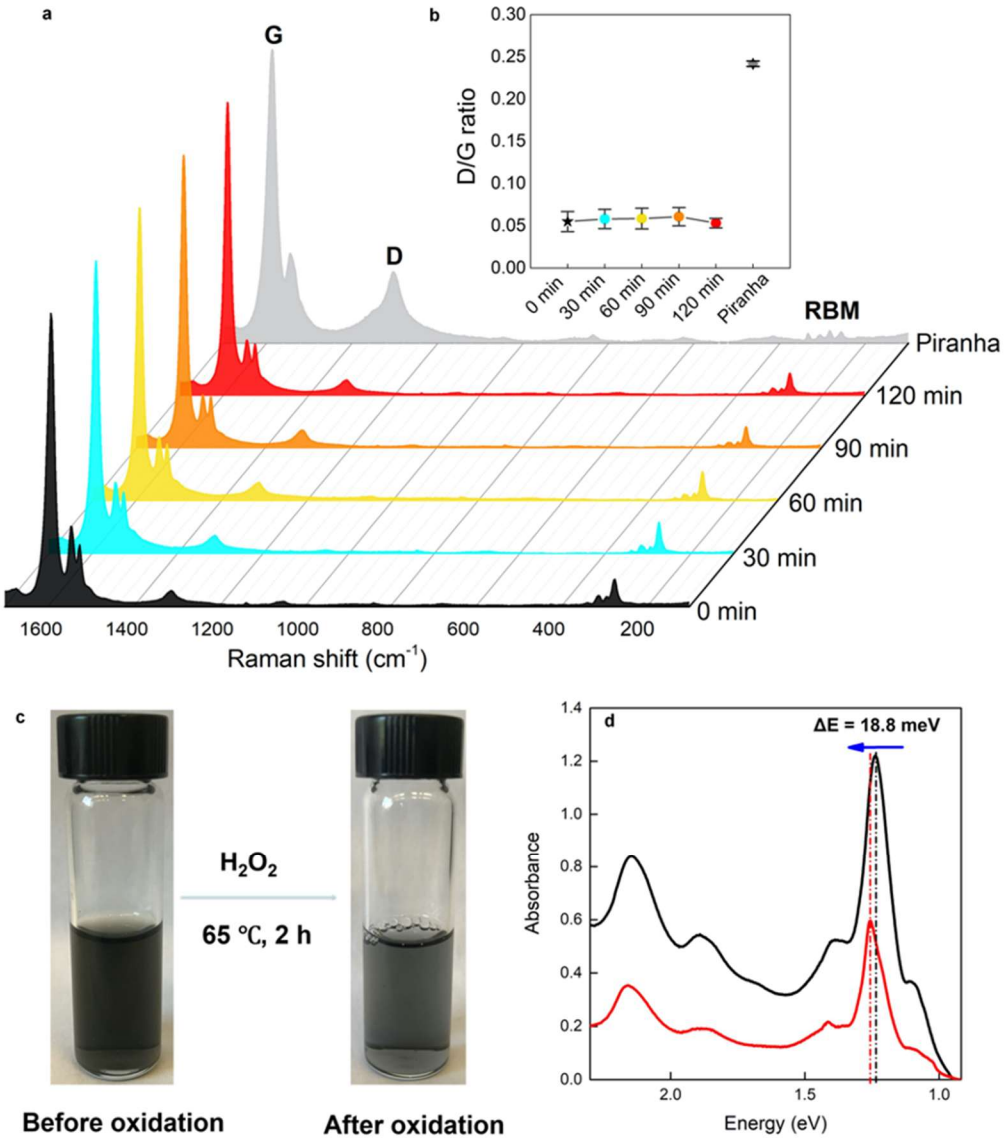

Figure 2-5. DICE retains the electronic structure of the starting nanotubes and achieves high yields. (a) Raman spectra of f+c-SWCNTs with different oxidation times of 0, 30, 60, 90, and 120 min. The excitation line is 633 nm. We included f-SWCNTs cut by piranha solution for 30 min for comparison. (b) Comparison of the D/G ratios of these samples. (c) Images of the f-SWCNT solution before and after the H_2O_2 cutting process for 120 min (both samples were dispersed in 4 mL 1 wt% DOC/H_2O). (d) UV-VIS-NIR absorption spectra of the f-SWCNTs before (black) and after (red) 120 min H_2O_2 oxidation.

2.3.3 Bright PL from Ultrashort Nanotubes in the Shortwave Infrared

The ultrashort nanotubes prepared by DICE maintain the E_{11} absorption features characteristic of SWCNTs (Figure 2-5d), indicating that this controllable cutting process keeps the electronic structure of the ultrashort nanotubes intact. In the excitation-emission PL map of the f+c-SWCNTs (120 min H_2O_2 oxidation) (Figure 2-6a), we observed E_{11} PL at 980 nm and E_{11}^- PL at 1150 nm from (6,5) nanotubes, which resonate with the same excitation wavelength of 580 nm, consistent with the brightening mechanism in which mobile excitons are trapped and locally emit as the defect-induced E_{11}^- PL. As proposed in Figure 2-1, E_{11} PL originates from the intact nanotube segments, which make up the body of the FUNs, and E_{11}^- PL is due to the added *p*-nitroaryl defects. As a control, we measured the PL of nanotubes synthesized by oxidatively cutting long pristine nanotubes in H_2O_2 for 2 h, 4 h, 6 h and 8 h (see the Experimental Section and Figure 2-7 for details) and found that the E_{11} PL became weaker as the oxidation proceeded, while no E_{11}^- PL was observed, which allowed us to conclude that the defect-induced E_{11}^- fluorescence observed in FUNs was indeed caused by the implanted *p*-nitroaryl defects. We also found that both E_{11} and E_{11}^- PL intensities of the f+c-SWCNTs decreased with oxidation time (Figure 2-6b). This decrease can be attributed to the consumption of the SWCNTs.[53]

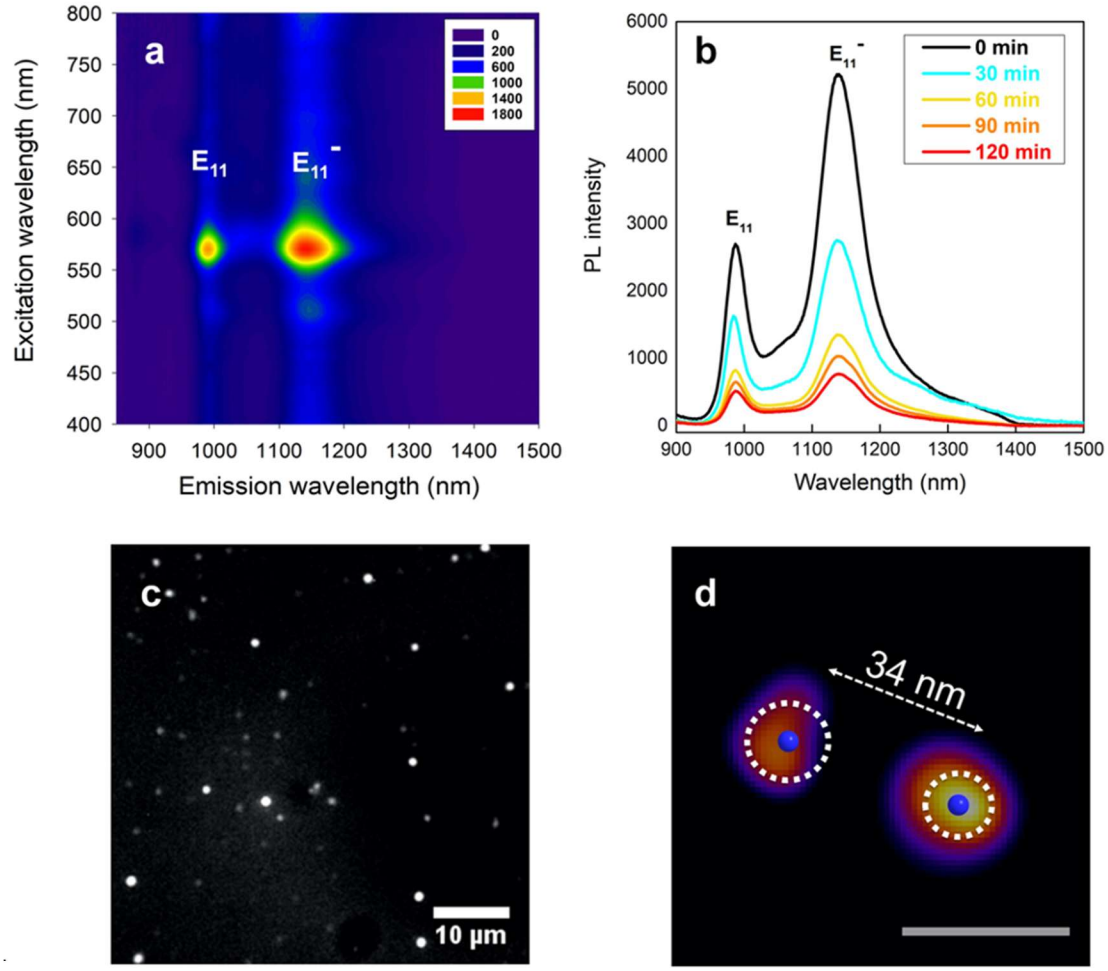

Figure 2-6. Bright PL from ultrashort nanotubes in the shortwave infrared. (a) An excitation-emission 2D PL map of the f+c-SWCNTs (120 min H_2O_2 oxidation) reveals the material's bright PL. (b) PL spectra of the f+c-SWCNTs made using different oxidation times (0 min, 30 min, 60 min, 90 min, and 120 min). (c) Broad band (900–1600 nm) PL images of f+c-SWCNTs (120 min H_2O_2 oxidation). All bright spots are diffraction limited. (d) The PL image of an ultrashort nanotube with defect locations super-resolved. Scale bar = 30 nm. The mean localization of a single defect is represented by a blue spot and the corresponding localization precision (~10 nm) by dotted circles.

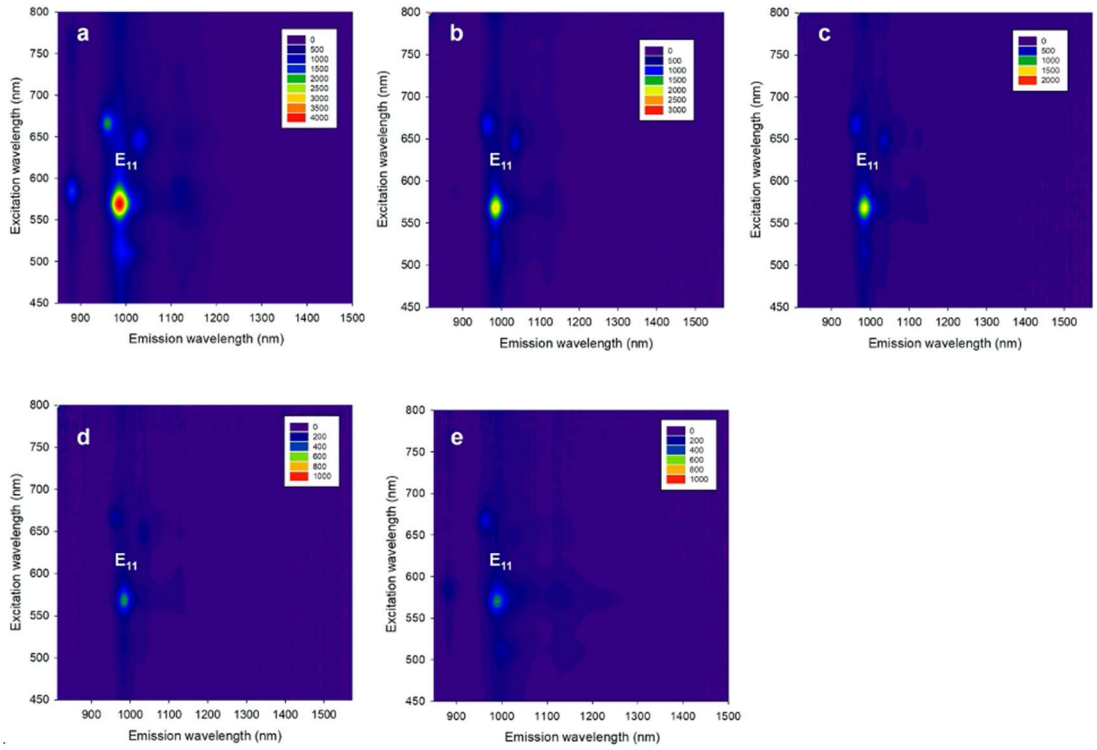

Figure 2-7. Characterization of the PL of pristine SWCNTs before and after oxidation with H_2O_2. Excitation-emission 2D PL maps of pristine SWCNTs (a) without and with (b) 2 h, (c) 4 h, (d) 6 h and (e) 8 h cutting by H_2O_2. After H_2O_2 oxidation, the E_{11} PL of the pristine SWCNTs became much weaker. No E_{11}^- PL was observed.

We further studied the PL at the individual nanotube level and performed single nanotube PL imaging of f+c-SWCNTs (120 min H_2O_2 oxidation). The nanotubes were dispersed in surfactant and drop-cast onto a polystyrene-Au-Si wafer substrate. The sample was then placed under an inverted microscope equipped with a liquid nitrogen-cooled InGaAs detector. We collected the broadband (900–1600 nm) PL images of individual nanotubes (Figure 2-6c) and observed bright PL from the sample, in which all fluorescent nanotubes appear as diffraction-limited spots. Due to the diffraction limit of optical microscopy, we cannot determine the length of these ultrashort SWCNTs based on the PL images. However, the defect location along the nanotube

length can be determined by super-localization analysis, as we recently reported. Figure 2-6d exemplifies a single ultrashort nanotube with two super-resolved defect sites separated by 34 nm. Figure 2-8 shows a histogram constructed from statistical analysis of 20 nanotubes, which gives a distance of 48 ± 8 nm between two defects. This distance approximately matches the nanotube length obtained from AFM (Figure 2-2e), suggesting the defects are located at the nanotube ends. This observation is in good agreement with the proposed cutting mechanism that oxidation preferentially takes place from implanted defect sites on the nanotube sidewalls, leaving *p*-nitroaryl groups on the ends of the cut nanotubes, which produce the observed defect PL.

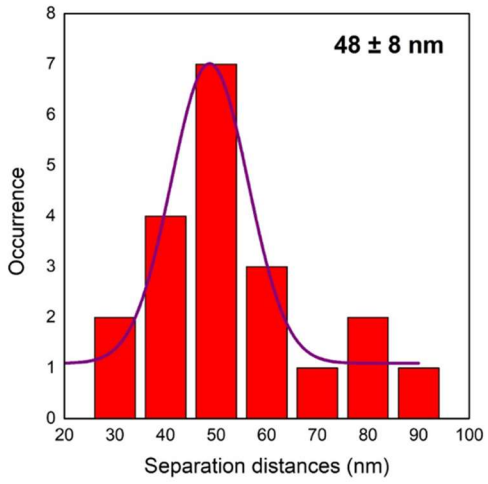

Figure 2-8. Histogram of the super-resolved separation distances between defects. The distribution of the separation distances between defects on the f+c-SWCNTs is comparable to the length distribution of the same sample (Figure 2e: 120 min H_2O_2 oxidation).

FT-IR spectroscopy also provides chemical information supporting this conclusion. Figure 2-9 is the IR spectrum of the f+c-SWCNTs (120 min H_2O_2 oxidation). We observed O-H stretching (3650–2900 cm^{-1}) and O-H bending at 1440–

1395 cm^{-1} and 1420–1330 cm^{-1} for carboxylic acid and alcohol, respectively. We also observed C-H stretching of aldehyde (2830-2695 cm^{-1}). The peak at approximately 1750–1550 cm^{-1} may include C=O stretching of an aldehyde (1740–1720 cm^{-1}), carboxylic acid (1720–1700 cm^{-1}), and ketone (1685–1666 cm^{-1}). We also noticed a broad peak of 1500–1250 cm^{-1}, which covers the N–O stretching (1550–1475 cm^{-1}, asymmetrical; 1360–1290 cm^{-1}, symmetrical) of the *p*-nitroaryl group, although the overlap with C-O stretching (1300 to 1250 cm^{-1}) makes it difficult to unambiguously assign this peak. We note that the chemical signatures of oxidized carbon nanotubes may be better resolved by near edge X-ray absorption fine structure spectroscopy.[36] However, FT-IR spectroscopy supports that DICE introduces oxygen-containing groups into FUNs, such as hydroxyls (-OH), aldehydes (-CHO), ketones (-C=O), and carboxylic acids (-COOH), while the *p*-nitroaryl group survives the DICE chemistry as indicated by the characteristic defect PL.[26, 31]

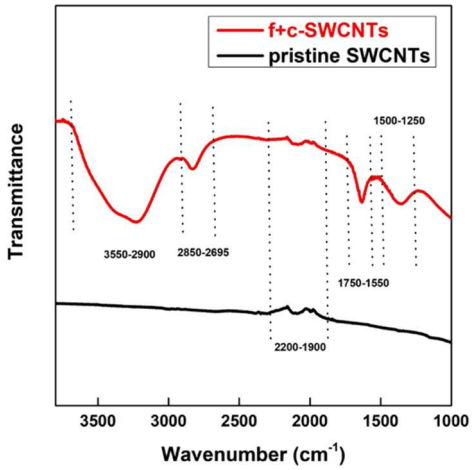

Figure 2-9. FT-IR spectra of pristine SWCNTs and f+c-SWCNTs (H_2O_2 oxidation for 2 h).

To completely rule out the possibility that the observed PL may come from a small fraction of long nanotubes, we correlated AFM and hyperspectral PL imaging at the single nanotube resolution by targeting the same region of interest on the sample substrate with the aid of fluorescent markers (Figure 2-10). The PL image is shown in Figure 2-10c along with a large-area AFM image locating the same area (Figure 2-10d). We further zoomed in on a smaller region of this same area (5 μm × 5 μm red boxes shown in Figure 2-10c and d, same region) and characterized it by AFM in tapping mode. As shown in Figure 2-10e, no long SWCNTs were observed, however, there were indeed several ultrashort SWCNTs, which correlate well with the PL image, confirming that the ultrashort SWCNTs produced by DICE are intensely fluorescent.

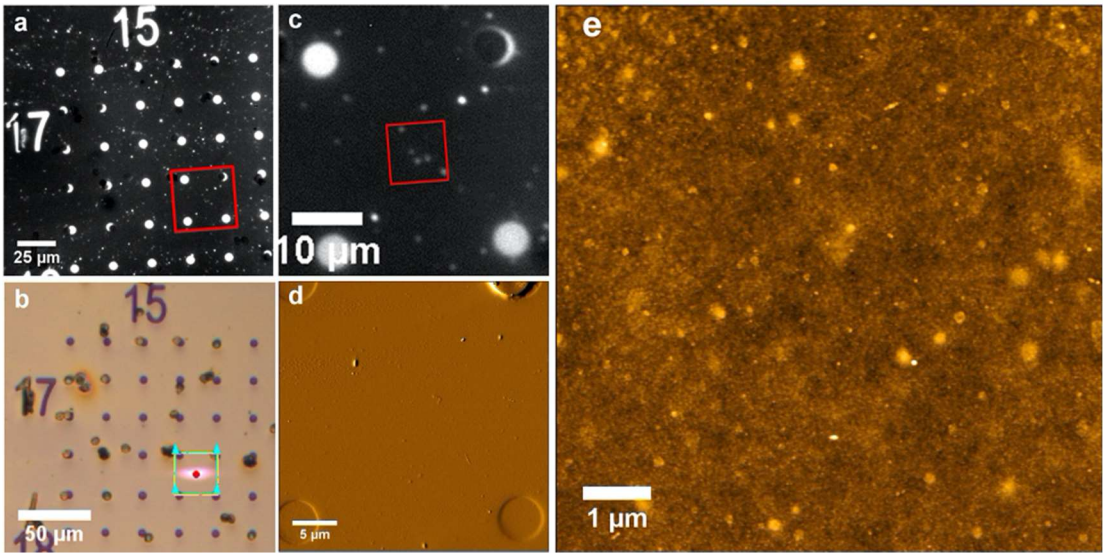

Figure 2-10. Correlated AFM and PL imaging measurement of FUNs. Low magnification (a) broad band (900–1600 nm) PL image of oxidized f+c-SWCNTs (2h H_2O_2 oxidation) and (b) an optical image from the AFM microscope in the same region of the sample. The box shows the region being magnified displayed in parts (c) and (d) of the figure. (c) High magnification PL image and (d) AFM height image in this region. The red box shows the further magnified region displayed in part (e) of the figure. (e) AFM height image in this region, in which no long nanotubes were observed.

2.3.4 Alternative Defect Implanting Chemistry for DICE

We found the defects for DICE can also be implanted by off-the-shelf diazonium salts in aqueous solution, demonstrating significant generality of our strategy. After the defect-implanting diazonium reaction in aqueous solution, the f-SWCNTs emit both E_{11} PL at ~980 nm and E_{11}^- PL at ~1150 nm (Figure 2-11a). After 2 h oxidative cutting in H_2O_2, the f+c-SWCNTs retain their E_{11} and E_{11}^- PL (Figure 2-11b). AFM measurements confirm that the carbon nanotubes were cut into short pieces (Figure 2-11c, d).

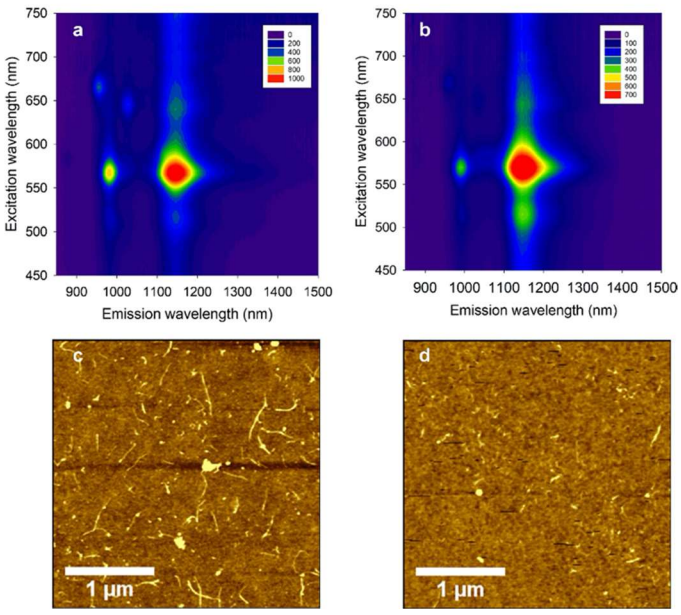

Figure 2-11. The defects for DICE can also be implanted by off-the-shelf diazonium salts in aqueous solution. The excitation-emission 2D PL maps of (a) f-SWCNTs functionalized with 4-nitrobezenediazounium tetrafluoroborate in aqueous solution and (b) the corresponding f+c-SWCNTs after 2 h H_2O_2 oxidation, revealing the materials' bright PL. Representative AFM height images of the (c) aqueous diazonium f-

SWCNTs and (d) f+c-SWCNTs (2 h H_2O_2 oxidation) demonstrates the effectiveness of the DICE strategy in synthesizing FUNs.

2.3.5 Quantum Chemical Computation Suggests that DICE Follows Charge-Enhanced Reactivity at the Defect Site

DICE features a highly selective cutting process induced by the introduction of sp^3 defect centers. The observed low defect levels of the synthesized FUNs, high yield, and acceleration of nanotube cutting all consistently provide evidence that chemical cutting occurs selectively from these defect sites. To better understand the high selectivity of DICE, we used Natural Population Analysis[42] to determine the charge distribution along the f-SWCNTs (see the Experimental Section for more details) and present the results in Figure 2-12. Note that C_1 is the sp^3 defect center connected to the *p*-nitroaryl functional group and C_2 is another sp^3 carbon atom next to C_1, connected to a hydrogen atom. While most of the carbons in the nanotube sidewall are close to neutral in charge ($|q| < 0.03$), we found that the charges of C_1 and C_2 are -0.074 and -0.264, respectively. The negative charges of C_1 and C_2 make the sp^3 carbons more reactive during oxidation as enriched free electrons largely favor oxidation attacks by hydroxyl radicals. We propose that oxidation of the f-SWCNT at the defect site breaks the bond between C_1 and C_2, followed by adding hydroxyl groups to both carbon atoms. We then applied Natural Population Analysis to this new model after bond breakage and the addition of hydroxyl groups, which showed that C_1 and C_2 becomes positively charged (0.198 and 0.051, respectively). In return, some of the carbon atoms surrounding the defect site now gain a negative charge (*e.g.*, C_3, -0.033), which makes

them more favorable targets for further oxidative cutting. This picture shows that the initially introduced *p*-nitroaryl group stays connected to C_1, which becomes an end atom of the resulting ultrashort nanotube. Figure 2-13 shows more detailed natural charge distribution maps for atoms near a defect site.

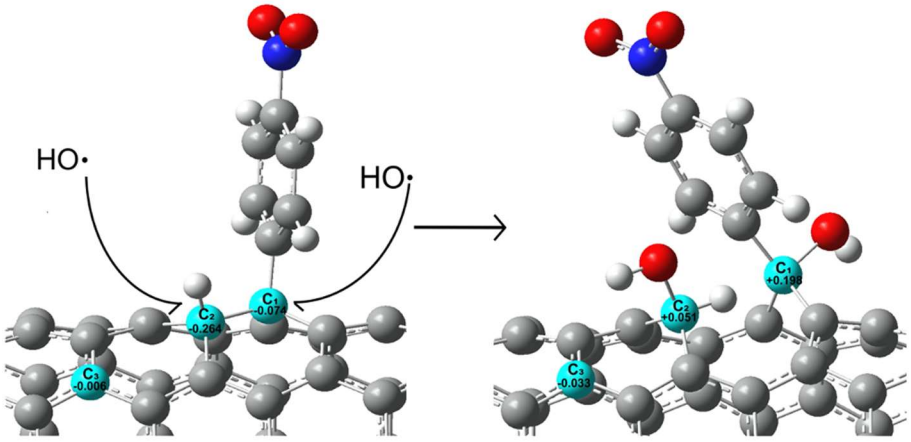

	Before breaking C_1-C_2 bond			After breaking C_1-C_2 bond		
Basis set	C_1	C_2	C_3	C_1	C_2	C_3
3-21G	-0.074	-0.264	-0.006	0.198	0.051	-0.033
6-31G	-0.071	-0.267	-0.006	0.223	0.066	-0.031

Figure 2-12. Quantum chemical computation suggests DICE follows charge-enhanced reactivity at the defect site. Natural Population Analysis shows charge distributions at the vicinity of a defect. Carbons of interest are highlighted and labeled C_1-C_3. Before the addition of hydroxyl groups, in the f-SWCNT the sp^3 carbons at the defect site, C_1 and C_2, are negatively charged while nearby carbons are effectively neutral. A hydroxyl radical will therefore selectively oxidize the defect site. After the addition of hydroxyl groups, C_1 and C_2 at the defect site acquire positive charges. Meanwhile, close to the defect, C_3 acquires a negative charge, making it a more favorable site for further oxidative cutting. The table below shows the basis set comparison of charges determined from Natural Population Analysis.

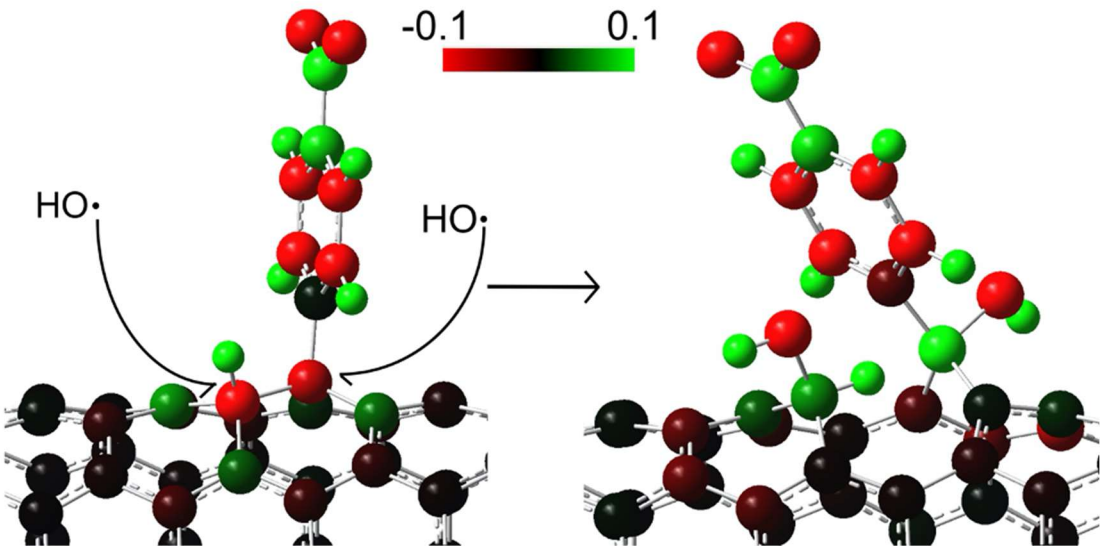

Figure 2-13. Natural charge distribution maps of atoms near a defect site in a f-SWCNT model. The same model is shown as in Figure 2-10, with atoms colored by charge as determined by Natural Population Analysis. Geometry optimization was performed with the B3LYP functional and 3-21G basis set.

2.4 Conclusions

We have addressed the synthetic challenge of fluorescent ultrashort nanotubes by implanting sp^3 chemical defects along the lengths of SWCNTs and subsequently cutting the structure at these defect centers with H_2O_2. We show that the introduced sp^3 defects not only accelerate the cutting process, but also enable the ultrashort nanotubes to fluoresce brightly in the shortwave infrared despite being significantly shorter than the diffusion length of excitons. The cut SWCNTs are ultrashort and feature a narrow length distribution (38 ± 18 nm) and low defect densities (D/G ~0.05). The chemistry is highly defect-selective, as shown by its high yield (~57%) and Natural Population Analysis of the material's charge distribution. This work makes FUNs available at synthetic quantities, opening opportunities for bio-imaging, bio-sensing, and

photophysics, as well as other applied and fundamental studies of fluorescent ultrashort nanotubes.

Chapter 3: In-situ Spectroscopic Study Reveals Two-stage Defect-induced Chemical Cutting of Carbon Nanotubes

3.1 Introduction

In Chapter 2, we demonstrated that DICE is an effective and facile method to synthesize FUNs at large scale with high yield. Both super-resolution imaging of defect locations at the single nanotube level and our natural population analysis of charge distribution on a nanotube results indicate that the hydroxyl radicals from hydrogen peroxide preferentially attack defect sites and then cut the nanotubes into shorter segments. However, more details about the DICE process remain to be explored. These unresolved questions include how the defect density and surfactant affect the reaction rate of DICE and the final length distribution of the product, and how this reaction evolves at different stages. In this chapter, we track the DICE reaction in situ using the absorption and defect-induced PL of SWCNTs as spectroscopic fingerprints. This in-situ spectroscopic study reveals a two-stage reaction mechanism (scission and etching), which allows us to precisely control the length distribution, functional degree, and PL intensity of the FUN product.

To synthesize FUNs (Figure 3-1), we first obtained single chirality (6,5)-SWCNTs from raw carbon nanotube materials by aqueous two-phase extraction (ATPE).[54] ATPE can efficiently remove metallic catalysts, non-nanotube carbon materials, and other chirality carbon nanotubes, preventing their interference in the absorption and PL spectra. Then we implanted *p*-nitroaryl functional groups on the purified (6,5)-SWCNTs in aqueous solution using diazonium chemistry,[55] which we can use to precisely monitor and control the nanotube defect density and functional degree. After functionalization, purified (6,5) f-SWCNTs with desired functional

degrees were obtained for the subsequent DICE process. We in-situ monitored the nanotube's absorption and PL spectral changes during H_2O_2 oxidation of the DICE reaction.

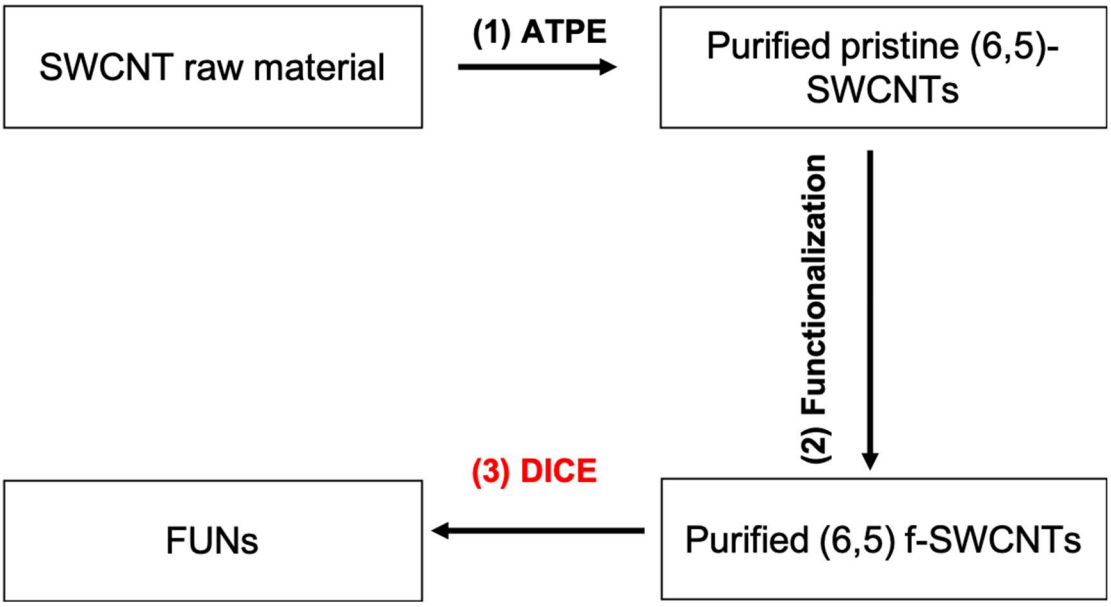

Figure 3-1. Schematic of the in-situ spectroscopic study of DICE. (1) Purified pristine (6,5) SWCNTs were extracted using the ATPE method from raw SWCNT materials. (2) Then we functionalized the pristine SWCNTs in aqueous solution by implanting p-nitroaryl groups on the nanotubes and synthesized purified (6,5) f-SWCNTs. (3) After functionalization, the (6,5) f-SWCNTs were oxidatively cut by H_2O_2 via the DICE reaction to produce FUNs, which we in-situ monitored to explore the reaction mechanism.

3.2 Experimental Methods

3.2.1 Sorting purified (6,5) SWCNTs using the ATPE Method

We conducted ATPE following the protocol reported by Duque et al.[54] CoMoCAT SG65i SWCNTs (≥ 99%, Lot No. SG65i-L39, SouthWest

NanoTechnologies; 1 mg) were dispersed in 1.04% (m/v) DOC/H_2O using tip sonication at 8 W for 1 h. Then the sonicated sample was ultracentrifuged at 16400 rpm for 2 h at 20 °C (Eppendorf centrifuge 5810R). Only the supernatant was collected for further separation.

In the first step of the ATPE process, we prepared the STOCK-1 solution, which contained 14.1 g of polyethylene glycol (PEG, MW 6000 Da, Alfa Aesar Lot no. 10173268), 4.9 g of dextran (MW 75000, Sigma-Aldrich), 0.49 g of sodium cholate (SC, Sigma-Aldrich), 1.117 g of SDS (Sigma-Aldrich), 0.142 g of NaCl (Sigma-Aldrich), and 100 g of nanopure water (Milli-Q-water). The STOCK-1 solution was mixed overnight with a magnetic stir bar to enable all the components to dissolve completely. Note that this STOCK-1 solution will phase separate, therefore it should be well mixed before use. 215 µL of the 1.04% DOC/H_2O SWCNT dispersion and 425 µL of nanopore water were added to 4080 µL of the STOCK-1 solution. This combined solution was then mixed using a vortex mixer and centrifuged for 5 min at 6000 g. We then collected the dark purplish bottom phase where the (6,5) SWCNTs concentrate (SP1-bottom). The first step of ATPE can effectively remove most non-fluorescent species.[54]

In the second step of ATPE, we prepared the STOCK-2 solution, which contained 14.5 g of PEG, 2.33 g of dextran, 0.0473 g of DOC (≥ 98%, Sigma-Aldrich), 1.8 g of SDS, and 100 g of nanopure water. Note that the STOCK-2 solution will phase separate, therefore mix it well before use. An equal amount of the SP1-bottom and STOCK-2 solution were mixed well with a vortex mixer, and then centrifuged for 5 min at 6000 g. Phase separation formed after centrifugation and we collected the top

phase where the (6,5)-SWCNTs concentrate (SP2-top). The bottom phase (SP2-bottom) contains (6,4) SWCNTs and can be stored for other uses.[54]

We then conducted dialysis to remove the remaining polymers in the collected solution using centrifugal ultrafiltration. A 100 kDa filtration membrane (Amicon Ultra-15 Centrifugal Filter Unit, 15 mL sample volume, UFC9100) was used in this process. In each centrifuge cycle (4000 rpm, 5 min), the samples were concentrated from 5 mL to ~500 μL and then diluted to 5 mL by adding 0.1 wt% DOC/H_2O. The centrifugation and dilution steps were repeated for more than five times to remove most residual polymers. After this process, we obtained purified (6,5)-SWCNTs dispersed in ~0.1 wt% DOC/H_2O. Note that we used low concentration DOC aqueous solution to facilitate the subsequent functionalization reaction as the diazonium salt can approach the nanotube surfaces more easily in a low concentration surfactant environment.

3.2.2 Functionalizing Pristine SWCNTs Using Diazonium Chemistry in Aqueous Solution

Following the purification process, we functionalized the (6,5)-SWCNTs using diazonium chemistry. We diluted the purified (6,5)-SWCNTs in 0.1 wt% DOC/H_2O stock solution using 0.1 wt% DOC/H_2O until the (6,5) nanotube optical density at E_{11} was lower than 0.5. Then 7.72 mg of 4-nitrobezenediazounium tetrafluoroborate powder (Sigma-Aldrich, 97%) was dissolved in 1 mL of H_2O, followed by a serial dilution (dilution factor = 1:1000). We added 30 μL of this diluted solution to 2 mL of the SWCNT solution in a cuvette, and then illuminated the cuvette with 565 nm light using a NanoLog spectrofluorometer (Horiba Jobin Yvon) while stirring the sample using a magnetic stir bar. We monitored the reaction in RTC mode. When the E_{11}^- PL

peak (~1150 nm) stopped increasing, we terminated the reaction by turning off the laser. This process was repeated 5 times to prepare ~10 mL of f-SWCNT solution. We can precisely prepare f-SWCNTs with targeted functional degree by tuning the amount of diazonium salt added to the nanotube solution.

3.2.3 In-situ Monitoring the DICE Reaction

After functionalization, we diluted the f-SWCNT sample using 1% SDS/H_2O to an optical density of less than 0.2 at the E_{11} absorption peak to avoid the inner filter effect.[56] We then added 1 mL of H_2O_2 (30 wt% in H_2O) to 1 mL of this f-SWCNT solution to conduct the DICE reaction. The mixed solution was loaded into a cuvette and placed in the Nanolog Spectrometer sample chamber. A water bath system was set to 70 ℃ to control the sample temperature. We capped the cuvette to avoid solution evaporation. The solution was heated in the sample chamber while being magnetically stirred. The PL spectra were collected on the NanoLog spectrofluorometer every 5 min. UV-VIS-NIR absorption spectra were collected by a spectrophotometer with a broadband InGaAs detector (Lambda 1050, PerkinElmer) every 30 min. We terminated the reaction after 7 h when the PL of the nanotubes completely disappeared.

3.2.4 DICE in Different Surfactants

In addition to SDS surfactant, we also studied the DICE reaction for SWCNTs suspended with DOC. After functionalization, we diluted the f-SWCNT in 0.1 wt% DOC/H_2O sample using 1% DOC/H_2O to an optical density of less than 0.2 at the E_{11} absorption peak to avoid the inner filter effect.[56] The same remaining protocols were then conducted as described in section 3.2.3, followed by this dilution step.

3.3 Results and Discussion

3.3.1 Fluorescent Purified (6,5) SWCNTs with Controllable Defect Densities

Figure 3-2a, b shows the absorption spectrum and 2D excitation-emission map of purified (6,5) SWCNTs after ATPE chirality purification. In the absorption spectrum (Figure 3-2a), the E_{11} (988 nm), E_{22} (575 nm), and E_{33} (350 nm) absorption peaks of (6,5) SWCNTs are annotated. The flat absorption baseline indicates that non-nanotube species have been successfully removed. Note that a trivial amount of other chirality carbon nanotubes remained, giving rise to the small peaks in the absorption spectrum. In the 2D PL map (Figure 3-2b), the E_{11} PL emission peak is located at 988 nm with an excitation of 565 nm. No other PL emission peaks were found in the map, which indicates the high purity of the product after the ATPE separation.

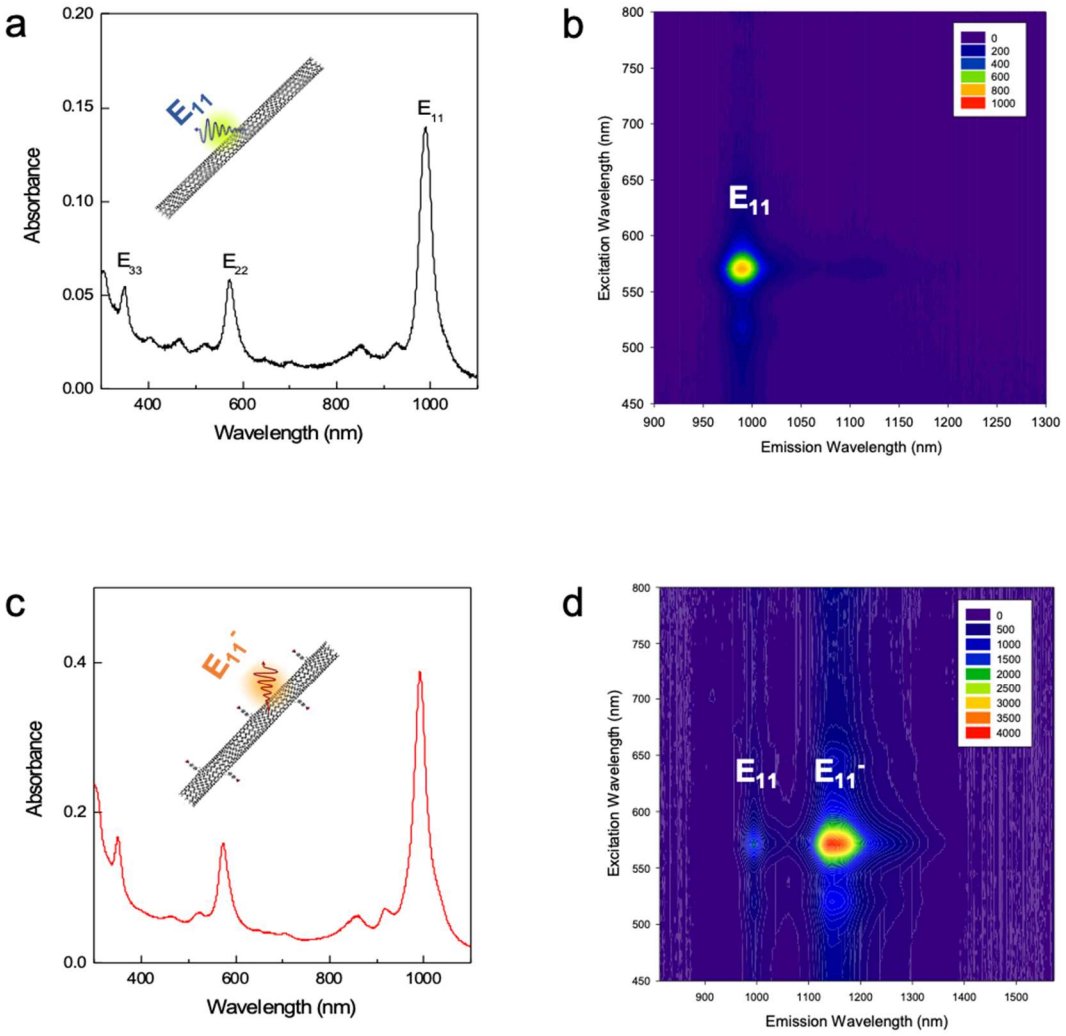

Figure 3-2. (a) Absorption spectrum and (b) 2D excitation-emission PL map of (6,5) SWCNTs purified by ATPE. (c) Absorption spectrum and (d) 2D excitation-emission PL map of purified (6,5) f-SWCNTs after introduction of covalent *p*-nitro-aryl defects using diazonium chemistry.

After functionalization using diazonium chemistry, the (6,5) chirality absorption peaks were retained in the f-SWCNTs (Figure 3-2c), indicating the electronic structure of the SWCNTs was not disrupted due to the introduction of covalent *p*-nitro-aryl defects. In the 2D PL map of the f-SWCNTs (Figure 3-2d), a new

E_{11}^- PL emission band appeared at ~1150 nm, which was redshifted from the E_{11} PL. The generation of this defect-induced PL demonstrates the successful synthesis of f-SWCNTs using diazonium chemistry in aqueous solution.[9, 26, 31, 55]

3.3.2 Two-Stage Reaction Mechanism

As the DICE reaction occurs on the f-SWCNTs, we in-situ monitored three key spectroscopic features: E_{11} absorbance, E_{11} PL intensity, and E_{11}^- PL intensity. The E_{11} absorbance is proportional to the concentration (number) of carbon atoms, which can be used as a direct index of the carbon consumption rate in the reaction.[12, 51] The E_{11}^- defect-induced PL intensity and the E_{11}^- / E_{11} intensity ratio are positively correlated to the number of fluorescent defects (i.e. *p*-nitroaryl defects in this study),[9, 26, 31, 55] and therefore provide information about the consumption rate of the fluorescent defects on the nanotubes.

We plotted the E_{11} absorbance change in the DICE reaction in Figure 3-3a and found that there are two distinct stages in this process. In the first stage (0–100 min), the E_{11} absorbance remained almost unchanged, indicating few carbon atoms were consumed. In the second stage (after ~100 min), the E_{11} absorbance drastically decreased due to the oxidation of carbon atoms to carbon dioxide in the presence of H_2O_2 while heating. These results suggested that SWCNT etching is mainly limited to this second stage of the reaction.

We also plotted the changes in the E_{11}^- PL intensity and E_{11}^- / E_{11} intensity ratio in Figure 3-3b-c, respectively. These values remained nearly unchanged at first (0–200 min), while began decreasing after ~200 min, again suggesting the presence of two

stages in the reaction. This observation indicates the defects were mainly consumed in the second stage as well.

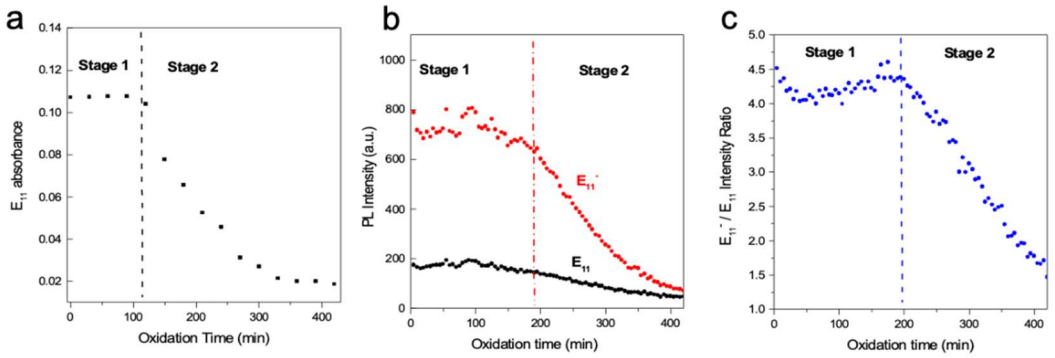

Figure 3-3. (a) The change in the E_{11} absorbance of the f-SWCNTs during the DICE reaction (SDS surfactant). The black dashed line divides the reaction in two stages. (b) E_{11} (black dots) and E_{11}^- (red dots) PL intensity change in the DICE reaction. The red dashed line divides the reaction in two stages. (c) E_{11}^- /E_{11} intensity ratio change in the DICE reaction. The blue dashed line divides the reaction in two stages.

The absorbance and PL intensity changes suggest a two-stage scission-then-etching reaction mechanism. In the first stage (the scission stage), the hydroxyl radicals preferentially attack the implanted defect sites on the SWCNTs, cutting the nanotubes at these locations. In this scission process, carbon atom loss is negligible, which explains why the E_{11} absorbance remains constant during this stage. The E_{11}^- PL intensity and the E_{11}^- / E_{11} intensity ratio remain unchanged either, suggesting that the number of defects does not decrease in this stage. These observations are strong evidence that long nanotubes are chopped to shorter fragments, but the defects survive as they are located on the ends of these cut nanotubes, confirming the FUN model we proposed in Chapter 2. In the second stage (the etching stage), after the long nanotubes have been chopped into shorter segments with defects at their ends, the number of

carbon nanotubes in the solution significantly increases. At this point, loss of carbon atoms due to H_2O_2 etching begins to dominate because of the increased number of etching reaction sites, i.e., the increased number of nanotube ends, where the etching reaction is known to occur.[46] We observed in the second stage, all indexes dropped drastically until all carbon atoms were consumed. This is a direct evidence that H_2O_2 can oxidize the carbon atoms to CO_2, destroying the defects located at the ends and continuously digesting through the length.

Another interesting observation is that the duration of the first stage in the E_{11}^- PL intensity change (200 min) is longer than that in the absorption change (100 min). This duration difference agrees with the fact that the cutting itself removes some carbon atoms and the fluorescent defects largely survive this cutting step. This duration difference allows us to shorten nanotubes without losing their defect-induced PL.

We also studied how the surfactant affects the DICE process by substituting SDS with DOC (see Experimental Methods section 3.2.4) and conducting the same in-situ monitoring experiments. In Figure 3-4a, we still observe a clear two-stage feature. The time period of the scission stage is from 0–60 min, and the etching stage occurs after 60 min. Figure 3-4b compares the change in the E_{11}^- / E_{11} intensity ratio for the different surfactants, demonstrating how they affect the reaction rate and duration of the two stages but do not alter the two-stage feature of the DICE reaction. DOC molecules have similar radius of SWCNT's curvatures and are known to pack on SWCNT along curvatures while leave the defect sites exposed to H_2O_2. In turn, SDS molecules form beaded structure at the nanotube surface and can cover the defect sites. This difference leads to a shorter stage 1, i.e., faster scission in DOC environment than

SDS. In addition, DOC molecules pack on SWCNTs more densely than SDS,[54] leaving fewer opening for H_2O_2 in the second stage, and therefore the E_{11} and E_{11}^- PL of the nanotubes decrease much slower in DOC than in SDS, a slower etching is observed.

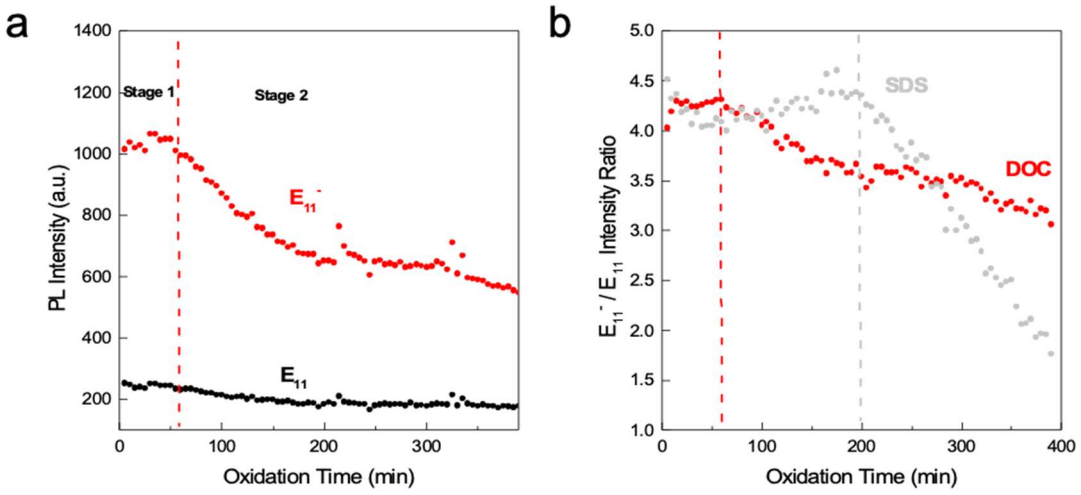

Figure 3-4. (a) E_{11} (black dots) and E_{11}^- (red dots) PL intensity change in the DICE reaction (DOC surfactant). The red dashed line divides DICE into two stages. (b) E_{11}^-/E_{11} intensity ratio change in the DICE reaction for different surfactants. DOC: red dots; SDS: grey dots. The red dashed line and grey dashed line annotate the turning points for the DOC and SDS conditions, respectively.

3.4 Conclusions

We explored the mechanism of the DICE reaction by in-situ monitoring changes in the absorption and PL spectra of (6,5) f-SWCNTs during the reaction process. We found that DICE is a two-stage reaction. In the first stage (scission), the hydroxyl radicals preferentially attack the previously implanted defect sites and cut the SWCNTs at these positions into shorter nanotubes segments, with the original defects at the ends. No significant carbon atoms or defect loss was observed in this stage. In the second stage (etching), the H_2O_2 etches the short nanotubes from the ends, leading

to a dramatic decrease in both the number of carbon atoms and defects. This phenomenon provides detailed molecular insights about the DICE reaction and allows us to predict and control the length distribution and PL intensity of FUNs in future syntheses. Further studies, including how the defect density impacts the reaction rate and the nanotube length distribution, and how the concentration of both reactants affects this reaction, are ongoing.

Chapter 4: Summary and Outlook

4.1 Summary

In this thesis, we have addressed the synthetic challenges of fluorescent ultrashort nanotubes. A defect-induced chemical cutting (DICE) chemistry reaction is proposed based on a fundamental new understanding of defect chemistry. The DICE reaction includes first implanting fluorescent quantum defects onto the nanotubes, and then oxidatively cutting the nanotubes selectively from the defect sites. The cut nanotubes were demonstrated to be ultrashort and fluorescent in shortwave infrared wavelengths.

Oxidation etching is widely used for nanocarbon. However, the molecular mechanism is largely unknown in part due to experimental difficulty in characterization. By in-situ monitoring the absorption and PL changes during DICE, we obtained direct experimental evidence that reveals a two-stage mechanism. In the first stage of the reaction (scission), the hydroxyl radicals preferentially attack the implanted defect sites and chop long nanotubes from the defect sites into short segments with defects on their ends, no significant carbon atoms or defects loss were observed. In the second stage (etching), the H_2O_2 etches the short nanotubes from the ends, leading to dramatic decrease of number of carbon atoms and defects.

In conclusion, this thesis reveals fundamental insights in defect chemistry and makes fluorescent ultrashort nanotubes synthetically accessible for both basic and applied studies. The work also opens the possibility to precisely predict and control the length distribution and functional degree of cut nanotubes in the synthesis.

4.2 Outlook for Fluorescent Ultrashort Nanotubes

4.2.1 Aqueous Solubility Enhancement through Structure Modifications

The aqueous solubility of SWCNTs is poor due to their hydrophobic nature. Surfactants such as SDS and DOC can disperse SWCNTs because of their amphiphilic properties. Superacids such as fuming sulfuric acid can disperse large amounts of SWCNTs by protonating them. Nevertheless, the reliance on surfactants or superacids limits the applications of SWCNTs in bio-imaging and medicine. Chemical methods using surface functionalization of SWCNTs can enhance wetting or adhesion characteristics and prevent them from aggregating in water, while aggressive chemical functionalization (strong acid, high temperature and etc.) can introduce structural defects and destroy the electronic structure of SWCNTs.[57]

Fluorescent ultrashort nanotubes can reach < 40 nm in length, and therefore the hydrophobic carbon cylinder is much shorter than long SWCNTs. In addition, H_2O_2 oxidation will introduce some hydrophilic hydroxyl groups to nanotube ends based on the proposed mechanism, which can contribute to enhancing nanotubes' aqueous solubility. The solubility of fluorescent ultrashort nanotubes can be further enhanced by functionalizing them with long and hydrophilic functional groups such as DNA chains or protein molecules, and these highly hydrophilic groups may dominate the solubility of nanotubes and make them aqueous soluble.

4.2.2 Potential Applications in Bioimaging and Sensing

The PL of fluorescent ultrashort nanotubes in the NIR-II window is ideal for biological imaging owing to the low autofluorescence and deep tissue penetration in this spectral region. In addition, the biocompatibility and toxicity of FUNs can be suppressed by shortening the nanotubes and enhancing their dispersity in aqueous solution.[13, 20, 22]

Further biotoxicity studies can be conducted first in mice experiments. After confirming their biocompatibility, FUNs may further enable bio-imaging and sensing experiments.

List of Publications

1. **Li, Y.**; Wu, X.; Kim, M.; Fortner, J.; Qu, H.; Wang, Y., Fluorescent Ultrashort Nanotubes from Defect-Induced Chemical Cutting. *Chemistry of Materials* 2019**,** *31* (12), 4536-4544.
2. Wang, P.;* **Li, Y.**;* Wang, L.; Klos, J.; Peng, Z.; Kim, N.; Bluhm, H.; Gaskell, K.; Liu, P.; Lee, S. B.; Eichhorn, B. W.; Wang, Y., Probing the Electrical Double Layer by *Operando* X-ray Photoelectron Spectroscopy through a Graphene-Carbon Nanotube Composite Window. *EcoMat,* Accepted. **(*equal contribution**)
3. Qu, H.; Rayabharam, A.; Wu, X.; Wang, P.; **Li, Y.**; Fagan, J.; Aluru, N. R.; Wang, Y., Selective Filling of n-Hexane in a Tight Nanopore. Submitted to *Nature Communication*, under peer review.

Bibliography

1. Miyauchi, Y., Photoluminescence studies on exciton photophysics in carbon nanotubes. *Journal of Materials Chemistry C* **2013,** *1* (40).
2. O'Connell, M. J.; Bachilo, S. M.; Huffman, C. B.; Moore, V. C.; Strano, M. S.; Haroz, E. H.; Rialon, K. L.; Boul, P. J.; Noon, W. H.; Kittrell, C.; Ma, J.; Hauge, R. H.; Weisman, R. B.; Smalley, R. E., Band gap fluorescence from individual single-walled carbon nanotubes. *Science* **2002,** *297* (5581), 593-6.
3. Wei, X.; Tanaka, T.; Yomogida, Y.; Sato, N.; Saito, R.; Kataura, H., Experimental determination of excitonic band structures of single-walled carbon nanotubes using circular dichroism spectra. *Nat Commun* **2016,** *7*, 12899.
4. Liu, J.; Rinzler, A. G.; Dai, H.; Hafner, J. H.; Bradley, R. K.; Boul, P. J.; Lu, A.; Iverson, T.; Shelimov, K.; Huffman, C. B.; Rodriguez-Macias, F.; Shon, Y. S.; Lee, T. R.; Colbert, D. T.; Smalley, R. E., Fullerene pipes. *Science* **1998,** *280* (5367), 1253-1256.
5. Chen, Z.; Kobashi, K.; Rauwald, U.; Booker, R.; Fan, H.; Hwang, W. F.; Tour, J. M., Soluble ultra-short single-walled carbon nanotubes. *J. Am. Chem. Soc.* **2006,** *128* (32), 10568-10571.
6. Sun, X.; Zaric, S.; Daranciang, D.; Welsher, K.; Lu, Y.; Li, X.; Dai, H., Optical properties of ultrashort semiconducting single-walled carbon nanotube capsules down to sub-10 nm. *J. Am. Chem. Soc.* **2008,** *130* (20), 6551-6555.
7. Tabakman, S. M.; Welsher, K.; Hong, G.; Dai, H., Optical Properties of Single-Walled Carbon Nanotubes Separated in a Density Gradient; Length, Bundling, and Aromatic Stacking Effects. *J. Phys. Chem.* **2010,** *114* (46), 19569-19575.
8. Gao, Z.; Oudjedi, L.; Faes, R.; Morote, F.; Jaillet, C.; Poulin, P.; Lounis, B.; Cognet, L., Optical detection of individual ultra-short carbon nanotubes enables their length characterization down to 10 nm. *Sci. Rep.* **2015,** *5*, 17093.
9. Danne, N.; Kim, M.; Godin, A. G.; Kwon, H.; Gao, Z.; Wu, X.; Hartmann, N. F.; Doorn, S. K.; Lounis, B.; Wang, Y.; Cognet, L., Ultrashort Carbon Nanotubes That Fluoresce Brightly in the Near-Infrared. *ACS Nano* **2018,** *12*, 6059-6065.
10. Kuang, Y.; Liu, J.; Sun, X., Ultrashort Single-Walled Carbon Nanotubes: Density Gradient Separation, Optical Property, and Mathematical Modeling Study. *J. Phys. Chem.* **2012,** *116* (46), 24770-24776.
11. Rajan, A.; Strano, M. S.; Heller, D. A.; Hertel, T.; Schulten, K., Length-dependent optical effects in single walled carbon nanotubes. *J. Phys. Chem. B* **2008,** *112* (19), 6211-6213.
12. Fagan, J. A.; Simpson, J. R.; Bauer, B. J.; Lacerda, S. H.; Becker, M. L.; Chun, J.; Migler, K. B.; Walker, A. R.; Hobbie, E. K., Length-dependent optical effects in single-wall carbon nanotubes. *J. Am. Chem. Soc.* **2007,** *129* (34), 10607-10612.
13. Smith, A. M.; Mancini, M. C.; Nie, S., Bioimaging: second window for in vivo imaging. *Nat. Nanotechnol.* **2009,** *4* (11), 710-711.
14. Welsher, K.; Liu, Z.; Sherlock, S. P.; Robinson, J. T.; Chen, Z.; Daranciang, D.; Dai, H., A route to brightly fluorescent carbon nanotubes for near-infrared imaging in mice. *Nat. Nanotechnol.* **2009,** *4* (11), 773-780.

15. Godin, A. G.; Varela, J. A.; Gao, Z.; Danne, N.; Dupuis, J. P.; Lounis, B.; Groc, L.; Cognet, L., Single-nanotube tracking reveals the nanoscale organization of the extracellular space in the live brain. *Nat. Nanotechnol.* **2017,** *12* (3), 238-243.
16. Yudasaka, M.; Yomogida, Y.; Zhang, M.; Tanaka, T.; Nakahara, M.; Kobayashi, N.; Okamatsu-Ogura, Y.; Machida, K.; Ishihara, K.; Saeki, K.; Kataura, H., Near-Infrared Photoluminescent Carbon Nanotubes for Imaging of Brown Fat. *Sci. Rep.* **2017,** *7*, 44760.
17. Antaris, A. L.; Robinson, J. T.; Yaghi, O. K.; Hong, G.; Diao, S.; Luong, R.; Dai, H., Ultra-low doses of chirality sorted (6,5) carbon nanotubes for simultaneous tumor imaging and photothermal therapy. *ACS Nano* **2013,** *7* (4), 3644-3652.
18. Iverson, N. M.; Barone, P. W.; Shandell, M.; Trudel, L. J.; Sen, S.; Sen, F.; Ivanov, V.; Atolia, E.; Farias, E.; McNicholas, T. P.; Reuel, N.; Parry, N. M.; Wogan, G. N.; Strano, M. S., In vivo biosensing via tissue-localizable near-infrared-fluorescent single-walled carbon nanotubes. *Nat. Nanotechnol.* **2013,** *8* (11), 873-880.
19. Weinberger, B.; Heck, D. E.; Laskin, D. L.; Laskin, J. D., Nitric oxide in the lung. *Pharmacol. Ther.* **1999,** *84* (3), 401-411.
20. Kolosnjaj-Tabi, J.; Hartman, K. B.; Boudjemaa, S.; Ananta, J. S.; Morgant, G.; Szwarc, H.; Wilson, L. J.; Moussa, F., In vivo behavior of large doses of ultrashort and full-length single-walled carbon nanotubes after oral and intraperitoneal administration to Swiss mice. *ACS Nano* **2010,** *4* (3), 1481-1492.
21. Antaris, A. L.; Chen, H.; Cheng, K.; Sun, Y.; Hong, G.; Qu, C.; Diao, S.; Deng, Z.; Hu, X.; Zhang, B.; Zhang, X.; Yaghi, O. K.; Alamparambil, Z. R.; Hong, X.; Cheng, Z.; Dai, H., A small-molecule dye for NIR-II imaging. *Nat. Mater.* **2016,** *15* (2), 235-242.
22. Kostarelos, K., The long and short of carbon nanotube toxicity. *Nat. Biotechnol.* **2008,** *26* (7), 774-776.
23. He, X.; Hartmann, N. F.; Ma, X.; Kim, Y.; Ihly, R.; Blackburn, J. L.; Gao, W.; Kono, J.; Yomogida, Y.; Hirano, A.; Tanaka, T.; Kataura, H.; Htoon, H.; Doorn, S. K., Tunable room-temperature single-photon emission at telecom wavelengths from sp3 defects in carbon nanotubes. *Int Conf Optic Mems* **2017,** *11* (9), 577-582.
24. Hogele, A.; Galland, C.; Winger, M.; Imamoglu, A., Photon antibunching in the photoluminescence spectra of a single carbon nanotube. *Phys. Rev. Lett.* **2008,** *100* (21), 217401.
25. Ishii, A.; Uda, T.; Kato, Y. K., Room-Temperature Single-Photon Emission from Micrometer-Long Air-Suspended Carbon Nanotubes. *Phys. Rev. Appl.* **2017,** *8* (5), 1-9.
26. Piao, Y.; Meany, B.; Powell, L. R.; Valley, N.; Kwon, H.; Schatz, G. C.; Wang, Y., Brightening of carbon nanotube photoluminescence through the incorporation of sp3 defects. *Nat. Chem.* **2013,** *5* (10), 840-845.
27. Kawabe, R.; Takaki, H.; Ibi, T.; Maeda, Y.; Nakagawa, K.; Maki, H., Pure and Efficient Single-Photon Sources by Shortening and Functionalizing Air-Suspended Carbon Nanotubes. *ACS Applied Nano Materials* **2019,** *3* (1), 682-690.

28. Siitonen, A. J.; Tsyboulski, D. A.; Bachilo, S. M.; Weisman, R. B., Surfactant-dependent exciton mobility in single-walled carbon nanotubes studied by single-molecule reactions. *Nano Lett.* **2010,** *10* (5), 1595-1599.
29. Crochet, J. J.; Duque, J. G.; Werner, J. H.; Lounis, B.; Cognet, L.; Doorn, S. K., Disorder limited exciton transport in colloidal single-wall carbon nanotubes. *Nano Lett.* **2012,** *12* (10), 5091-5096.
30. Kamalasanan, K.; Gottardi, R.; Tan, S.; Chen, Y.; Godugu, B.; Rothstein, S.; Balazs, A. C.; Star, A.; Little, S. R., "Zero-dimensional" single-walled carbon nanotubes. *Angew. Chem. Int. Ed.* **2013,** *52* (43), 11308-11312.
31. Kwon, H.; Furmanchuk, A.; Kim, M.; Meany, B.; Guo, Y.; Schatz, G. C.; Wang, Y., Molecularly Tunable Fluorescent Quantum Defects. *J. Am. Chem. Soc.* **2016,** *138* (21), 6878-6885.
32. Brozena, A. K., M.J.; Powell, L. R.; Wang, Y. H., Controlling the optical properties of carbon nanotubes with organic color-center quantum defects. *Nat. Rev. Chem.* **2019,** *in press*.
33. Vichchulada, P.; Cauble, M. A.; Abdi, E. A.; Obi, E. I.; Zhang, Q.; Lay, M. D., Sonication Power for Length Control of Single-Walled Carbon Nanotubes in Aqueous Suspensions Used for 2-Dimensional Network Formation. *J. Phys. Chem.* **2010,** *114* (29), 12490-12495.
34. Ziegler, K. J.; Gu, Z.; Peng, H.; Flor, E. L.; Hauge, R. H.; Smalley, R. E., Controlled oxidative cutting of single-walled carbon nanotubes. *J. Am. Chem. Soc.* **2005,** *127* (5), 1541-1547.
35. Shuba, M. V.; Paddubskaya, A. G.; Kuzhir, P. P.; Maksimenko, S. A.; Ksenevich, V. K.; Niaura, G.; Seliuta, D.; Kasalynas, I.; Valusis, G., Soft cutting of single-wall carbon nanotubes by low temperature ultrasonication in a mixture of sulfuric and nitric acids. *Nanotechnology* **2012,** *23* (49), 495714.
36. Lucas, A.; Zakri, C.; Maugey, M.; Pasquali, M.; van der Schoot, P.; Poulin, P., Kinetics of Nanotube and Microfiber Scission under Sonication. *J. Phys. Chem. C* **2009,** *113* (48), 20599-20605.
37. Tunuguntla, R. H.; Escalada, A.; V, A. F.; Noy, A., Synthesis, lipid membrane incorporation, and ion permeability testing of carbon nanotube porins. *Nat Protoc* **2016,** *11* (10), 2029-2047.
38. Kuznetsova, A.; Popova, I.; Yates, J. T.; Bronikowski, M. J.; Huffman, C. B.; Liu, J.; Smalley, R. E.; Hwu, H. H.; Chen, J. G. G., Oxygen-containing functional groups on single-wall carbon nanotubes: NEXAFS and vibrational spectroscopic studies. *J. Am. Chem. Soc.* **2001,** *123* (43), 10699-10704.
39. Williams, R. M.; Lee, C.; Galassi, T. V.; Harvey, J. D.; Leicher, R.; Sirenko, M.; Dorso, M. A.; Shah, J.; Olvera, N.; Dao, F.; Levine, D. A.; Heller, D. A., Noninvasive ovarian cancer biomarker detection via an optical nanosensor implant. *Sci. Adv.* **2018,** *4* (4), eaaq1090.
40. Wu, X.; Kim, M.; Qu, H.; Wang, Y., Single-defect spectroscopy in the shortwave infrared. *Nat Commun* **2019,** *10* (1), 2672.
41. Frisch, M. J. T., G. W.; Schlegel, H. B.; Scuseria, G. E.; Robb, M. A.; Cheeseman, J. R.; Scalmani, G.; Barone, V.; Mennucci, B.; Petersson, G. A.; et al. *Gaussian 09*, Gaussian, Inc.: Wallingford, CT, 2009.

42. Reed, A. E.; Weinstock, R. B.; Weinhold, F., Natural population analysis. *J. CHEM. PHYS.* **1985,** *83* (2), 735-746.
43. Hudson, J. L.; Casavant, M. J.; Tour, J. M., Water-soluble, exfoliated, nonroping single-wall carbon nanotubes. *J. Am. Chem. Soc.* **2004,** *126* (36), 11158-11159.
44. Kim, M.; Wu, X.; Ao, G.; He, X.; Kwon, H.; Hartmann, N. F.; Zheng, M.; Doorn, S. K.; Wang, Y., Mapping Structure-Property Relationships of Organic Color Centers. *Chem* **2018,** *4* (9), 2180-2191.
45. Allen, B. L.; Kotchey, G. P.; Chen, Y.; Yanamala, N. V.; Klein-Seetharaman, J.; Kagan, V. E.; Star, A., Mechanistic investigations of horseradish peroxidase-catalyzed degradation of single-walled carbon nanotubes. *J. Am. Chem. Soc.* **2009,** *131* (47), 17194-17205.
46. Wang, Y.; Shan, H.; Hauge, R. H.; Pasquali, M.; Smalley, R. E., A highly selective, one-pot purification method for single-walled carbon nanotubes. *J. Phys. Chem. B* **2007,** *111* (6), 1249-1252.
47. Garcia-Lastra, J. M.; Thygesen, K. S.; Strange, M.; Rubio, A., Conductance of sidewall-functionalized carbon nanotubes: universal dependence on adsorption sites. *Phys. Rev. Lett.* **2008,** *101* (23), 236806.
48. Lopez-Bezanilla, A.; Triozon, F.; Latil, S.; Blase, X.; Roche, S., Effect of the chemical functionalization on charge transport in carbon nanotubes at the mesoscopic scale. *Nano Lett.* **2009,** *9* (3), 940-944.
49. Dresselhaus, M. S.; Jorio, A.; Saito, R., Characterizing Graphene, Graphite, and Carbon Nanotubes by Raman Spectroscopy. *Annu. Rev. Condens. Matter Phys.* **2010,** *1* (1), 89-108.
50. Ziegler, K. J.; Gu, Z.; Shaver, J.; Chen, Z.; Flor, E. L.; Schmidt, D. J.; Chan, C.; Hauge, R. H.; Smalley, R. E., Cutting single-walled carbon nanotubes. *Nanotechnology* **2005,** *16* (7), S539-44.
51. Schöppler, F.; Mann, C.; Hain, T. C.; Neubauer, F. M.; Privitera, G.; Bonaccorso, F.; Chu, D.; Ferrari, A. C.; Hertel, T., Molar Extinction Coefficient of Single-Wall Carbon Nanotubes. *J. Phys. Chem. C* **2011,** *115* (30), 14682-14686.
52. Venema, L. C., Imaging Electron Wave Functions of Quantized Energy Levels in Carbon Nanotubes. *Science* **1999,** *283* (5398), 52-55.
53. Hertel, T.; Himmelein, S.; Ackermann, T.; Stich, D.; Crochet, J., Diffusion limited photoluminescence quantum yields in 1-D semiconductors: single-wall carbon nanotubes. *ACS Nano* **2010,** *4* (12), 7161-7168.
54. Subbaiyan, N. K.; Cambre, S.; Parra-Vasquez, A. N.; Haroz, E. H.; Doorn, S. K.; Duque, J. G., Role of surfactants and salt in aqueous two-phase separation of carbon nanotubes toward simple chirality isolation. *ACS Nano* **2014,** *8* (2), 1619-28.
55. Li, Y.; Wu, X.; Kim, M.; Fortner, J.; Qu, H.; Wang, Y., Fluorescent Ultrashort Nanotubes from Defect-Induced Chemical Cutting. *Chemistry of Materials* **2019,** *31* (12), 4536-4544.
56. Powell, L. R.; Piao, Y.; Ng, A. L.; Wang, Y., Channeling Excitons to Emissive Defect Sites in Carbon Nanotube Semiconductors beyond the Dilute Regime. *J. Phys. Chem. Lett.* **2018,** *9* (11), 2803-2807.
57. Vaisman, L.; Wagner, H. D.; Marom, G., The role of surfactants in dispersion of carbon nanotubes. *Adv Colloid Interface Sci* **2006,** *128-130*, 37-46.